Geochemistry
Geophysics
Geosystems
G^3
AN ELECTRONIC JOURNAL OF THE EARTH SCIENCES
Published by AGU and the Geochemical Society

Article
Volume 5, Number 12
31 December 2004
Q12C04, doi:10.1029/2003GC000603
ISSN: 1525-2027

Numerical investigation of layered convection in a three-dimensional shell with application to planetary mantles

David Oldham and J. Huw Davies

School of Earth, Ocean and Planetary Sciences, Cardiff University, Main Building, Park Place, Cardiff CF10 3YE, UK (dave@earth.cf.ac.uk; huw@earth.cardiff.ac.uk)

[1] Stratified stable layered mantle convection in a three-dimensional (3-D) spherical shell is investigated for a range of depth of layer, intrinsic density contrast between the layers ($\Delta\rho$), and heating mode. Three heating modes are studied: internal heating, bottom heating across core-mantle boundary, and both combined. For each heating mode, layers were investigated centered at depths from 500 km to 2500 km in 500 km steps and with $\Delta\rho$ from 1 to 5% in 1% steps. We did not find stable layering for $\Delta\rho$ of 1%. Cases with no bottom heating were stable with $\Delta\rho$ of 2%, but $\Delta\rho$ of at least 3% were required by cases with a component of bottom heating. All cases with $\Delta\rho$ of 4% or more were stable. We found that the stability of the layer is strongly dependent on the buoyancy ratio B ($B = \Delta\rho \div \rho\alpha\Delta T$, where $\Delta\rho$ is the chemical density increase across the boundary, ρ is the density in the upper layer, α is the thermal expansivity and ΔT is the radial temperature difference across the whole system) with a dense layer becoming unstable $B \approx 0.5$. We characterize the height and length scale of the undulations and the area of the interface. Deformations of the interface are largest for cases in which interface is in the midmantle and for cases with small density contrasts. We find that the heating mode does not affect the thermal structure of the layered system, which can be explained with energy balance considerations. The amplitude of the interfacial deformation is found to be unaffected by the heating mode and can be predicted using B. Our results suggest the interfacial thermal boundary layers require large temperature contrasts; therefore the lack of evidence for thermal boundary layers in global seismology studies between 500 and 2500 km depth suggests interfaces at these depths are unlikely.

Components: 13,611 words, 11 figures, 4 tables.

Keywords: chemical; convection; heat; layered; mantle; plumes.

Index Terms: 8121 Tectonophysics: Dynamics, convection currents and mantle plumes; 8124 Tectonophysics: Earth's interior—composition and state (1212); 8130 Tectonophysics: Heat generation and transport.

Received 17 July 2003; **Revised** 24 May 2004; **Accepted** 21 July 2004; **Published** 31 December 2004.

Oldham, D., and J. H. Davies (2004), Numerical investigation of layered convection in a three-dimensional shell with application to planetary mantles, *Geochem. Geophys. Geosyst.*, *5*, Q12C04, doi:10.1029/2003GC000603.

Theme: Thermochemical Convection in the Earth's Interior
Guest Editors: Peter van Keken, Louis Moresi, and Adrian Lenardic

1. Introduction

[2] While it has been proposed since the early days of continental drift [*Holmes*, 1928] and plate tectonics [*McKenzie*, 1969] that mantle convection drives surface motions, the geometry and details of the flow are still controversial [*Davies*, 1999; *Kellogg et al.*, 1999; *Tackley*, 2000]. Over the years there have been arguments for whole mantle convection (where it convects as a single body) and for layered convection (where there is intrinsic density contrast keeping two layers convecting

separately). Supporters of layered convection have placed the interface between the layers at a range of depths, including (1) the depth of the step in seismic velocity at ~660 km depth [*Richter and McKenzie*, 1981; *Allegre*, 2002; *O'Nions et al.*, 1979; *DePaolo and Wasserburg*, 1976], (2) a depth of around 1000 km [*Wen and Anderson*, 1995, 1997], (3) a depth of 1500–2000 km [*Kellogg et al.*, 1999], and (4) a depth of 2500–2700 km, D″ [*Lay et al.*, 1998; *Hofmann and White*, 1982].

[3] Some of the strongest arguments for a layered mantle have come from the geochemical community. The need for the mantle to consist of at least two reservoirs that have been isolated for ~2 Gyr, has been long discussed [*Hoffmann*, 1997; *Zindler and Hart*, 1986]. This and rare gas arguments based on ^{40}Ar [*Allegre et al.*, 1996] and He, including that insufficient ^{4}He is being released compared to the heat output [*O'Nions and Oxburgh*, 1983], have, among others, been used to argue for layering but with little constraint on geometry. Arguments for a chemical interface centered at around 660 km depth have included the facts that it is the maximum depth of deep earthquakes [*Richter and McKenzie*, 1981], that it corresponds to a large increase in seismic velocity and density, and that it seemed to match the reservoir volumes required by the earliest geochemical mantle evolution models based on Nd and Sr isotopes [*DePaolo and Wasserburg*, 1976]. Arguments for an interface in the shallow lower mantle, can be motivated by the work of *Montagner* [1994], *Wen and Anderson* [1995, 1997], and *Kawakatsu and Niu* [1994]. The arguments for an interface in the deeper lower mantle (~1400–2000 km) have included the loss of slab continuity [*van der Hilst and Karason*, 1999], and the mismatch of heat generation from MORB source with the surface heat flux [*Kellogg et al.*, 1999]. Seismology, including seismic reflections, velocity discontinuities, scattering, anisotropy and velocity anomalies have been used as arguments for an unique region at the base of the mantle [*Lay et al.*, 1998].

[4] Other models to try and explain geochemical reservoirs excluding layers have included blobs [*Davies*, 1984; *Becker et al.*, 1999]; recycling, thermo-chemical convection [*Hoffmann*, 1997]; and possibly inputs from the core [*Brandon et al.*, 1998]. This work cannot address these classes of models.

[5] Geophysical arguments against present-day layering have come from tomography, [*Grand et al.*, 1997; *van der Hilst et al.*, 1997]; including inverse correlation of long wavelength geoid with lower mantle seismic heterogeneity [*Hager et al.*, 1985; *Richards and Hager*, 1984] extended to dynamic surface topography, CMB ellipticity, and plate velocities [*Forte et al.*, 2002], subdued mid-ocean ridge topography [*Davies*, 1988], and lack of global continuous seismic reflectors away from depths of accepted phase transitions at 410 and 670 km depth [*Vidale et al.*, 2001]. *Helffrich and Wood* [2001] have combined geochemical and seismic arguments to argue for whole mantle convection. While *Ballentine et al.* [2002] argued that the rare gas case for layering does not exist if the Helium concentration in the mantle has been underestimated by a factor of 3.5. *Van Keken et al.* [2002] in a review on mixing related to geochemical heterogeneity feel that no single model is able to account for all the major observations. Some geochemists have argued that since all the strong evidence for whole mantle convection is from present-day whereas many of the strong arguments for layering are geochemical, based on the integration of behavior over a long period of time; that in fact the Earth was a layered system in the past but has now transitioned to a single layer system [*Allegre*, 2002].

[6] To more rigorously test the various possibilities for layered convection, one needs predictions for the expected characteristics of such convection, including for example the level of intrinsic density difference needed for stability and the quantification of the interfacial deformation. For example in deciding the likelihood that seismic reflections are observable off an interface one would like to know the slope of such an interface, and also whether topography allows such a step to disappear in one-dimensional (1-D) radial models.

[7] Models of layered mantle convection have included numerical and laboratory models. Early numerical models had a flat, impermeable interface [e.g., *Richter and McKenzie*, 1981; *Ellsworth and Schubert*, 1988; *Cserepes and Rabinowicz*, 1985]. One of the first works with a deformable interface is that of Christensen and Yuen which was in two-dimensional (2-D) Cartesian geometry [*Christensen and Yuen*, 1984], followed by *Davies and Gurnis* [1986]. A valuable benchmark paper for thermo-chemical convection was published comparing different numerical techniques [*Van Keken et al.*, 1997]. Others who have undertaken numerical models of layered convection with a deformable interface include *Kellogg et al.* [1999], *Montague and Kellogg* [2000], *Tackley and Xie* [2002], *Tackley* [2002], and *Lenardic and Kaula* [1993], while laboratory experiments have included *Cardin*

and Nataf [1991], *Cardin et al.* [1991], *Davaille* [1999a, 1999b]; *Le Bars and Davaille* [2002], *Gonnermann et al.* [2002], *Jellinek et al.* [2002], *Jellinek and Manga* [2002], and *Namiki and Kurita* [2003]. We would like to point out that our work here does not address layering generated by negative Clapeyron slope of the 660 km phase transition [e.g., *Machetel and Weber*, 1991], nor general thermo-compositional convection where there is mixing and not just simple stratification [e.g., *Christensen and Hofmann*, 1994]. There is a large literature in both fields, including three-dimensional (3-D) spherical simulations [*Tackley et al.*, 1993; *Stegman et al.*, 2002a, 2002b].

[8] Here we present the first work we are aware of that systematically investigates layered convection in 3-D spherical geometry with a deformable interface. *Glatzmaier and Schubert* [1993] have undertaken such 3-D spherical geometry models with an impermeable, isothermal interface. The advantage of modeling the system in a 3-D spherical geometry is that the geometric properties of the layers will scale in a planetary like manner as the radius of the interface is varied. The volume (e.g., total heat generated in the lower layer through internal heating) will scale with r^3; while the surface area (e.g., area over which heat can be conducted out of the lower layer) will scale with r^2. Results will therefore be geometrically comparable to a mantle-like system.

[9] The modeling of layered mantle convection presented includes a survey of the effect of (1) the depth of the interface allowing the results to be used to discuss, traditional 660 km layering, through midmantle to lowermost mantle layering; (2) a range of intrinsic density contrasts, from 1% to 5%, and (3) three modes of heating, basal, internal and a combination. After describing the simulations, and their results, we discuss their possible implications for the geometry of mantle convection.

2. Layered Convection in Spherical Geometry

[10] The different methods for modeling layered convection include (1) the field method, where a field is introduced to represent composition and a conservation of composition equation is solved, very similar to the conservation of energy equation, (2) the particle method, here the compositional field is carried by particles which are advected by the flow, the density of particles within a region allows its composition to be evaluated, (3) and a marker method, where markers representing the boundary are followed around the flow and are used to reconstruct the location of the boundary. Since we are interested in stable layered systems the marker method is applicable and potentially the most suitable since out of the above methods it has the lowest numerical diffusivity for composition [*Van Keken et al.*, 1997].

[11] In the marker method one keeps track of which side a node is of the marker defined interface. The marker population needs to be controlled to maintain a good distribution. This is achieved by combining markers in regions of excess and generating markers in regions of low concentrations. The marker method becomes computationally very expensive when the layers get well mixed, but since we were only interested in studying cases of stratified layering this was not a disadvantage. The marker chain method has until very recently only been employed in 2-D calculations [*Christensen and Yuen*, 1984]. Applying a marker method in 3-D is more complex. The term "chain" is no longer accurate, and ''marker net'' is perhaps less misleading terminology. The significance of moving from a chain to a net is that markers are not stored in a linear array and it is not trivial to find the appropriate neighbor to each marker. It is though possible to track the boundary in detail with sophisticated interpolation [*Schmalzl and Loddoch*, 2003] and then process the results to provide the body forces. This allows very complex deformation to be followed. Given our interest in only simulating stratified systems, we do not need to follow such extreme deformation and therefore avoid the work in tracking and interpolating the surface but develop a method that leads directly to an efficient representation of the compositional field from the tracked markers. The standard equations for conservation of mass, momentum and energy [*Bunge et al.*, 1997] are solved using the code TERRA [*Baumgardner*, 1983; *Yang*, 1997]. It solves the equations using a finite element discretization [*Baumgardner*, 1985] on an icosahedral grid [*Baumgardner and Frederickson*, 1985] and has been parallelized [*Bunge and Baumgardner*, 1995] for efficient solution of large problems. A summary of the marker method employed can be found in Appendix A, and a series of validation test are presented in Appendix B.

[12] Layered systems with a mantle-like geometry were simulated with three different heating modes. In the first mode only internal heating was present

Table 1. Parameters of Numerical Simulations[a]

Parameter	Variable	Value
Outer shell radius	R_S	6.370×10^6 m
Inner shell radius	R_{CMB}	3.500×10^6 m
Depth of marker surface	D_K	500, 1000, 1500, 2000, and 2500 km
Temperature of surface	T_S	1060 K
Temperature of CMB (with bottom heating)	T_{CMB}	3000 K
Temperature of CMB (with no bottom heating)	T_{CMB}	No temperature constraints–insulating
Density of the upper layer	ρ_u	5.00×10^3 kg m^{-3}
Density of the lower layer	ρ_l	5.05, 5.10, 5.15, 5.20 and 5.25 $\times 10^3$ kg m^{-3}
Density contrast	$\Delta\rho/\rho$	1, 2, 3, 4, and 5%
Dynamic viscosity	η	4.125×10^{23} Pa s
Rate of internal heating (with internal heating)	q_{rad}	0.450×10^{-12} W kg^{-1}
Rate of internal heating (bottom heating only)	q_{rad}	0.0 W kg^{-1}
Thermal conductivity	k	2.4 W m^{-1} K^{-1}
Gravitational acceleration	g	10 m s^{-2}
Volume coefficient of thermal expansion	α	2.0×10^{-5} K^{-1}
Specific heat at constant volume	C_V	1×10^3J kg^{-1} K^{-1}
Thermal diffusivity	κ	4.8×10^{-7} m^2 s^{-1}

[a] The parameters used in the calculations presented in this paper. The effects of varying the depth of the deformable boundary and the density of the lower layer were studied, and several values are listed for these parameters. Different heating modes were also used, and in the cases with no bottom heating the lower boundary was insulating.

to drive convection (e.g., simulating radioactivity and/or secular cooling). In these cases the value of the local internal heating (W kg^{-1}) was kept the same in both the upper and lower layers. A boundary condition of zero heat flux was applied at the lower shell boundary. Consequently while the heat energy generated per unit volume within the lower layer was constant for each case simulated the total energy generated in the lower layer varied with its volume. In the second heating mode only bottom heating was active (simulating heating by the core across the core-mantle boundary (CMB)). In these cases the temperature of the CMB was kept fixed at 3000 K. Since the internal temperature and the thickness of the thermal gradient at the CMB varied, so too did the heat energy entering the lower layer in this mode. The third mode was a combination of the previous two modes; that is, it had both internal and bottom heating applied. Again in these cases the total heat entering the system varied between cases. In this mode the local heat generation rate was constant, and the temperature of the CMB temperature was fixed at 3000 K. For the cases with bottom heating the Bénard Rayleigh number would be 1.448×10^5 if the convection extended over the whole mantle; while the internal heating Rayleigh number for the whole mantle for appropriate cases would be 5.762×10^5. Since the system is layered such Rayleigh numbers have no meaning for the actual individual layers in these calculations. The separate layers would individually have lower Rayleigh numbers, the exact values controlled largely by the different shell thicknesses. The ratio of radii of the inner and outer shell boundaries is similar to Earth's mantle. Other physical parameters used are listed in Table 1.

[13] For each heating mode at least 12 cases were simulated with the average depth of the interface and the chemical density contrast across it being varied. All the cases undertaken are listed in Table 2.

[14] In the cases presented the Boussinesq approximation was used for an incompressible fluid. The viscosity, thermal conductivity and the volume coefficient of thermal expansion were kept constant with depth. The velocity boundary condition on both the upper and lower shells was free slip. A grid with 1,310,720 nodes was used with an internode spacing of ~100 km.

[15] The simulations presented here deviate from Earth-like values in a number of ways. The vigor of convection is two to three orders of magnitude lower than that estimated in Earth's mantle.

[16] To produce an initial case for each heating mode, a simple, low-degree, spherical harmonic temperature field was introduced into a system without a deformable boundary. Once a quasi steady state was reached and all trace of the original spherical harmonic field had gone, a deformable boundary was introduced as a spherical surface at the depth of interest.

[17] The controlling parameter in layered convection is the ratio of chemical to thermal buoyancy:

Table 2. Summary of Results of Numerical Simulations[a]

Heating Mode	Depth, km	$(\Delta\rho/\rho)$%	Stable?	ΔT_K, K	B	$(\Delta\rho/\rho)_{eff}$%	Mrk SD, km	Area Variable φ
Internal	500	1	no	-	-	-	-	-
Internal	500	2	yes	699	1.02	0.60	113	0.042
Internal	500	3	yes	816	1.31	1.37	71	0.017
Internal	500	4	yes	826	1.74	2.35	47	0.007
Internal	500	5	yes	837	2.15	3.33	37	0.006
Internal	1000	1	no	-	-	-	-	-
Internal	1000	2	yes	514	1.16	0.97	278	0.161
Internal	1000	3	yes	552	1.61	1.90	93	0.050
Internal	1000	4	yes	582	2.15	2.84	76	0.027
Internal	1000	5	yes	575	2.67	3.85	56	0.014
Internal	1500	2	no	-	-	-	-	-
Internal	1500	2	yes	333	1.35	1.33	136	0.093
Internal	1500	3	yes	340	1.90	2.32	75	0.025
Internal	1500	4	yes	339	2.54	3.32	47	0.010
Internal	1500	5	yes	336	3.18	4.33	35	0.006
Internal	2000	1	no	-	-	-	-	-
Internal	2000	2	yes	195	1.27	1.61	203	0.076
Internal	2000	3	yes	173	1.95	2.65	97	0.021
Internal	2000	4	yes	172	2.62	3.66	69	0.011
Internal	2000	5	yes	166	3.31	4.67	52	0.007
Internal	2500	1	no*	-	-	-	-	-
Internal	2500	2	yes*	47	1.70	1.91	202	0.084
Internal	2500	3	yes*	42	2.57	2.92	127	0.034
Internal	2500	4	yes*	54	3.38	3.89	102	0.017
Bottom	500	2	no	-	-	-	-	-
Bottom	500	3	no	-	-	-	-	-
Bottom	500	4	yes	713	1.03	2.57	203	0.072
Bottom	500	5	yes	775	1.25	3.45	170	0.055
Bottom	1000	2	no		-	-		-
Bottom	1000	3	yes	735	0.77	1.53	456	0.340
Bottom	1000	4	yes	801	1.03	2.40	308	0.135
Bottom	1000	5	yes	800	1.25	3.40	200	0.074
Bottom	1500	2	no	-	-	-	-	-
Bottom	1500	3	yes	783	0.77	1.43	525	0.686
Bottom	1500	4	yes	851	1.03	2.30	328	0.244
Bottom	1500	5	yes	920	1.29	3.16	187	0.110
Bottom	2000	2	no		-	-		-
Bottom	2000	3	yes	870	0.77	1.26	419	0.490
Bottom	2000	4	yes	942	1.03	2.12	198	0.163
Bottom	2000	5	yes	1019	1.29	2.96	104	0.048
Bottom	2500	2	no*	-	0.52	-	-	-
Bottom	2500	3	no*	-	0.77	-	-	-
Bottom	2500	4	yes*	996	1.03	2.01	294	0.222
Both	500	2	no	-	0.52	-	-	-
Both	500	3	yes	784	0.77	1.43	347	0.384
Both	500	4	yes	1088	1.03	1.82	198	0.107
Both	500	5	yes	1169	1.29	2.66	116	0.030
Both	1000	2	no	-	0.52	-	-	-
Both	1000	3	yes	895	0.77	1.21	485	0.559
Both	1000	4	yes	996	1.03	2.01	323	0.191
Both	1000	5	yes	1035	1.29	2.93	162	0.062
Both	1500	2	no	-	0.52	-	-	-
Both	1500	3	yes	768	0.77	1.46	553	0.755
Both	1500	4	yes	878	1.03	2.24	322	0.280
Both	1500	5	yes	933	1.25	3.13	183	0.089
Both	2000	2	no	-	0.52	-	-	-
Both	2000	3	yes	774	0.77	1.45	460	0.581
Both	2000	4	yes	835	1.03	2.33	211	0.172
Both	2000	5	yes	866	1.29	3.27	119	0.045
Both	2500	2	no	-	0.52	-	-	-
Both	2500	3	no	-	0.77	-	-	0.693

Table 2. (continued)

Heating Mode	Depth, km	$(\Delta\rho/\rho)$%	Stable?	ΔT_K, K	B	$(\Delta\rho/\rho)_{eff}$%	Mrk SD, km	Area Variable φ
Both	2500	4	yes*	751	1.03	2.50	238	0.189
Internal-Hot	2000	5	yes	1004	2.01	2.99	70	0.020

[a] Here "both" describes cases in which both internal radiogenic heating and bottom heating were present. Depth describes the depth at which the deformable interface is centered. $(\Delta\rho/\rho)$% is the chemical density increase as a percentage across the interface, the lower layer always being denser. ΔT_K is the temperature across the deformable interface (see Figure 2). B is the global buoyancy ratio defined in equation (1); note this uses the temperature contrast across the whole system ΔT (not ΔT_K). For cases with bottom heating the temperature contrast over the whole mantle is an input parameter and so B can be evaluated even for unstable cases. However, for internally heated cases the temperature across the whole mantle is an output parameter, and B for unstable cases is unknown. $(\Delta\rho/\rho)_{eff}$% is the effective density contrast across the interface once the effects of thermal expansion have been accounted for (see equation (2)). The area variable φ is defined in equation (5). The standard deviation of the markers' height represents the amplitude of undulation of the deformable interface. Simulations where the surface defined by the markers is pressed against either the upper or lower boundary are represented by an asterisk (*) beside the stable value.

This is described by the buoyancy ratio B defined by *Davaille* [1999a] as

$$B = \frac{\Delta\rho}{\rho\alpha\Delta T}, \tag{1}$$

where $\Delta\rho$ is the intrinsic chemical density difference between the two layers, ρ is the reference density, α is the thermal expansion coefficient and ΔT is the temperature contrast across the system. From her laboratory experiments, Davaille characterizes the behavior of such a system in Cartesian geometry based on its global buoyancy ratio B and the viscosity ratio of the two layers. The position of our experiments on her graph is shown in Figure 1. From this we expect our results to be stratified and in cases when the layer does become unstable no doming regime should develop.

3. Results

[18] When considering the results of these simulations it is important to remember that these systems presented here are stable layered cases with heat energy being transported across the interface between the two layers only by thermal conduction. When the deformable interface is introduced convection is taking place across the whole mantle and there is no thermal boundary between the two layers. Consequently, the topology of the interface quickly develops with large domes where plumes are rising through the mantle and low-lying regions in areas of subduction. A thermal boundary develops and the system works toward a stable thermal state. After this initial rapid distortion, the amplitude of domes and troughs tends toward a quasi-steady value in the stratified cases; while some of the cases with lower intrinsic density contrasts become unstable.

[19] Initially the lower layer is unable to lose heat via conduction across the deformable boundary at

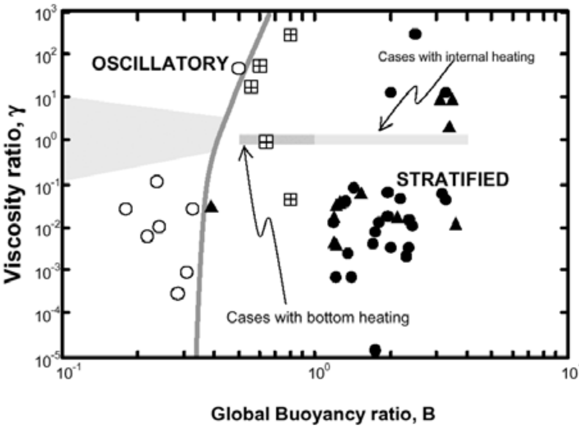

Figure 1. The behavior of layered convecting systems as a function of the buoyancy ratio B and the viscosity ratio γ for 3-D Cartesian geometry adapted from Figure 2 of *Davaille* [1999a]. The location of our experiments on the graph (labeled with mode of heating) shows that we expect to be in the stratified regime for B > 0.5. The gray vertically striped line shows the experiments in which bottom heating is present. In these cases the buoyancy ratio is defined entirely by input parameters and so can itself be considered an input parameter. The gray diagonally striped line shows experiments in which only internally heating was present. The temperature of the CMB was able to vary during the experiment. As a result, the temperature contrast across the mantle changed. The values of the buoyancy ratio presented here use the temperature contrast once the system has reached a steady state. For these internally heated cases the buoyancy ratio must be thought of as an output value of the experiment. Each symbol represents one of Davaille's experiments. Open circles, where domes filled the tank; filled circles, two-layer convection with plumes rising from the interface; patterned squares, a hybrid regime with severe topography and plumes; triangles, cases where one layer was too thin to convect. The gray region is the domain where a doming mode is not present and the layers immediately mix.

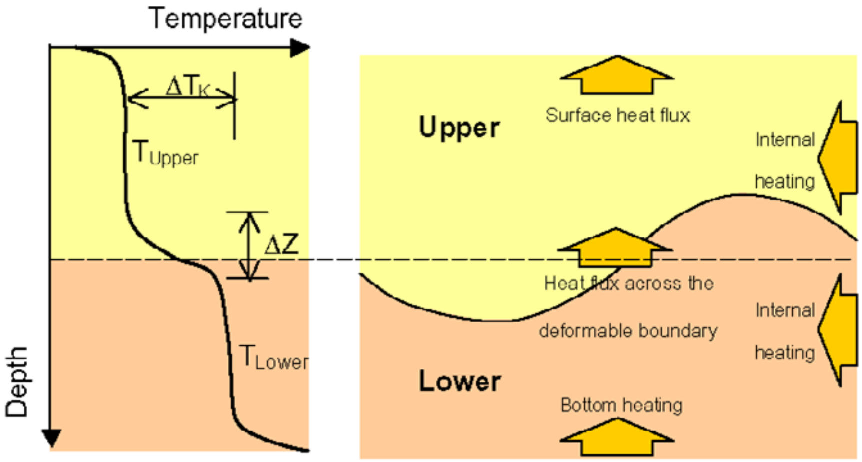

Figure 2. A schematic of the thermal structure in the layered case. We define ΔT_K as the thermal contrast across the deformable boundary. For a bottom-heated system to exist in a quasi steady state, the heat crossing the CMB, the deformable boundary and the surface must be equal.

the same rate it is being advected to the boundary by convection (at least for the cases which have a supercritical lower layer). As a consequence the temperature rises in the lower layer and the thermal gradient across the interface becomes larger allowing more heat to be conducted. The temperature continues to rise in the lower layer until quasi-thermal equilibrium is reached. Similarly a thermal boundary layer develops at the base of the upper layer. A schematic of the radial thermal structure at quasi-steady state is shown in Figure 2.

[20] The time evolution of a combined heating mode case, with an interface centered at 1500 km depth and $\Delta\rho$ = 4%, toward quasi-steady state is illustrated in Figure 3. We note that the time evolution is steady, with a thermal boundary of around 350 K; and taking around 200 Gyr to reach full steady state, but with the majority of the adjustment taking just 50–100 Gyr.

[21] The deformation of the interface also tends toward a quasi steady state. Figures 4a and 4b

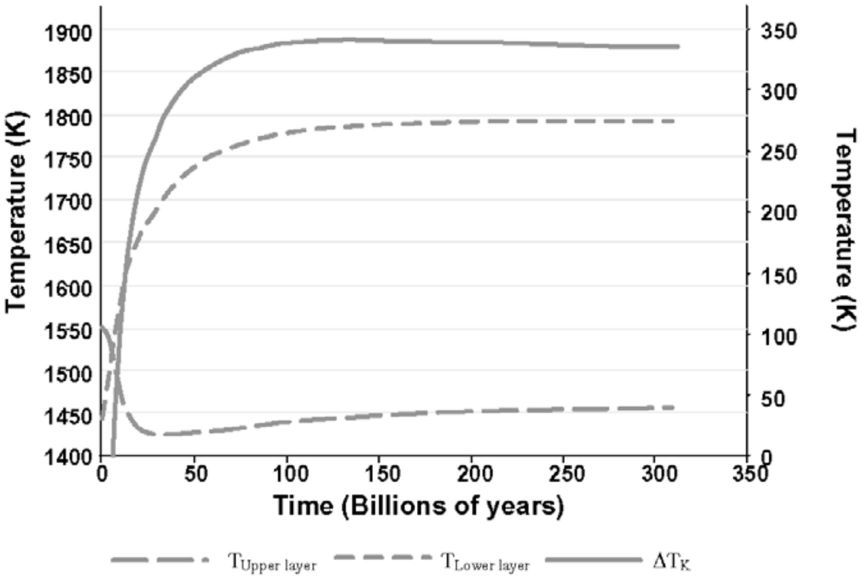

Figure 3. The thermal evolution of a case with both internal and bottom heating with a 4% chemical density increase over the deformable boundary centered at a depth of 1500 km. The temperature of the upper and lower layers (T_{upper} and T_{lower}) is plotted on the left axis; the temperature contrast $\Delta T_K = (T_{lower} - T_{upper})$ is plotted on the right axis.

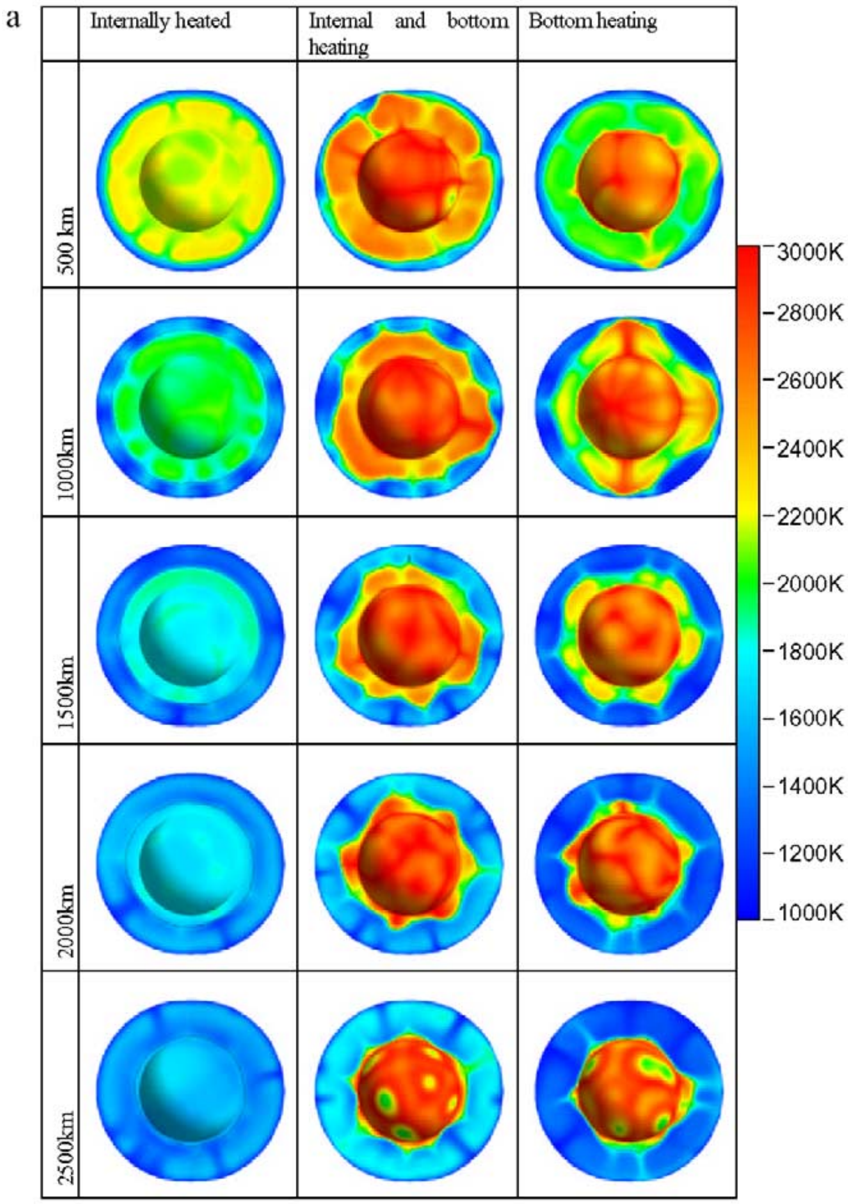

Figure 4. Temperature fields for cases with a 4% density increase across the deformable interface. All three heating modes are shown for the five different depths at which the layer's boundary was modeled. (a) The total temperature field. (b) The temperature field with the radial average temperature removed. (c) The interfacial topography. The color scale represents height above the mean height of the interface in kilometers.

illustrate the thermal structure at one moment in the quasi steady state, while Figure 4c illustrates the interfacial structure at the same time.

[22] When different density contrasts were investigated for the same depth of boundary and heating mode, the system, as expected, became more stable for larger density contrasts. Features on the interface between the two layers are very long-lived and survive several overturns of either layer. This may be explained by the relatively low vigor of convection in our simulations and the effect this has on fixing the position of upwelling and downwelling features produced at thermal boundaries.

[23] For the internally heated cases the amplitude of the interface's undulations reached a maximum for the cases where the layer was at 1000 km depth. At this depth (actually around 1050 km) the volume of the two layers is equal with each being 50% of the total volume of the mantle. For cases with bottom heating the interface undulations were

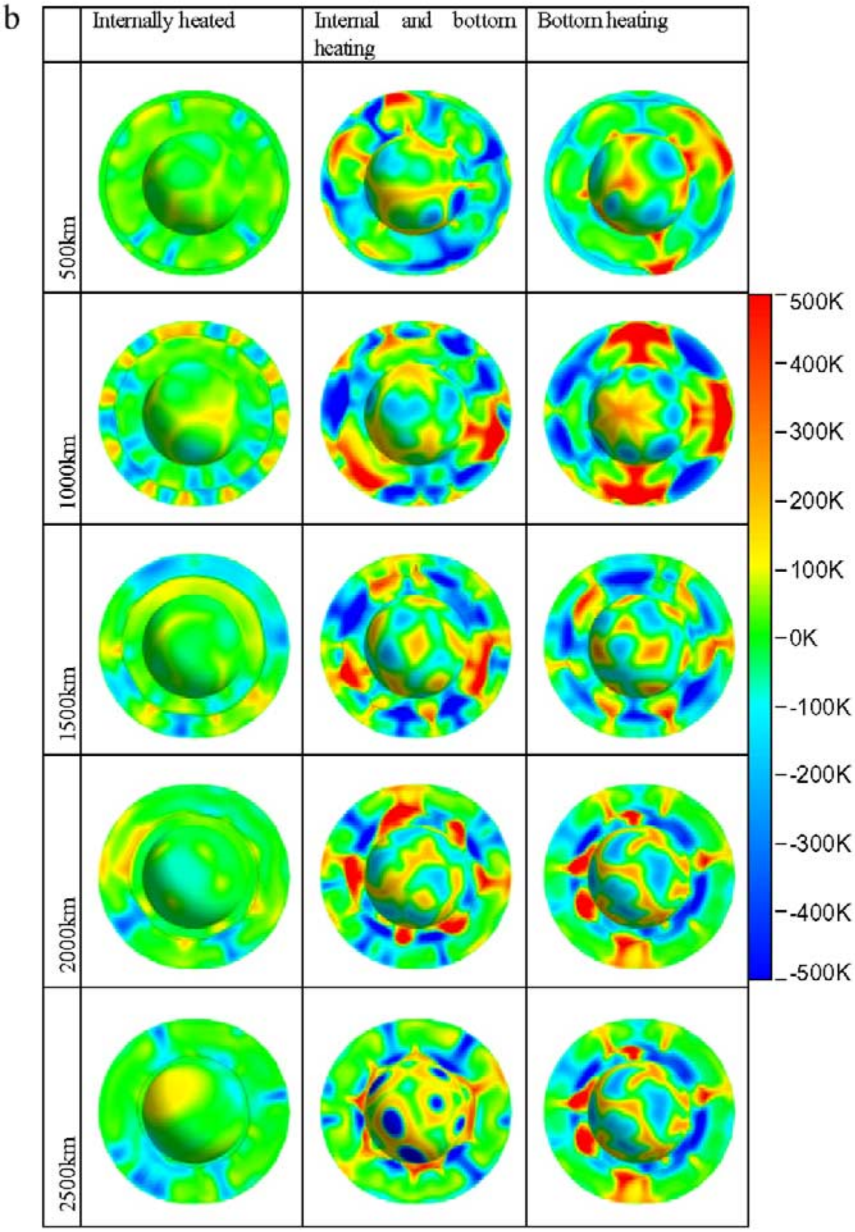

Figure 4. (continued)

greatest when it was centered at the midmantle depth of 1500 km.

[24] High peaks in the deformable boundary had two forms. The first was a large dome that had a hot region below it and was caused by the buoyant uprising of the hot material. The second were cusped ridge structures that were caused by the presence of cold subducted material above the boundary. Cold material that had descended in slab form from the surface built up in "packets" over the deformable boundary and often caused depressions in it. Where two of these packets pressed together the deformable boundary was squeezed into a cusped ridge. When the interface was centered at 500 km depth the cusps point downward, and the reverse for interface centered at 2500 km. At the other depths, both up and down pointing cusps are present.

[25] For bottom-heated cases the total heat entering the lower layer ranged between 1.567×10^{12} W and 2.192×10^{12} W with the most heat being added in cases when the chemical boundary was deeper in the mantle and had a smaller density contrast across it. This variation in heat input was

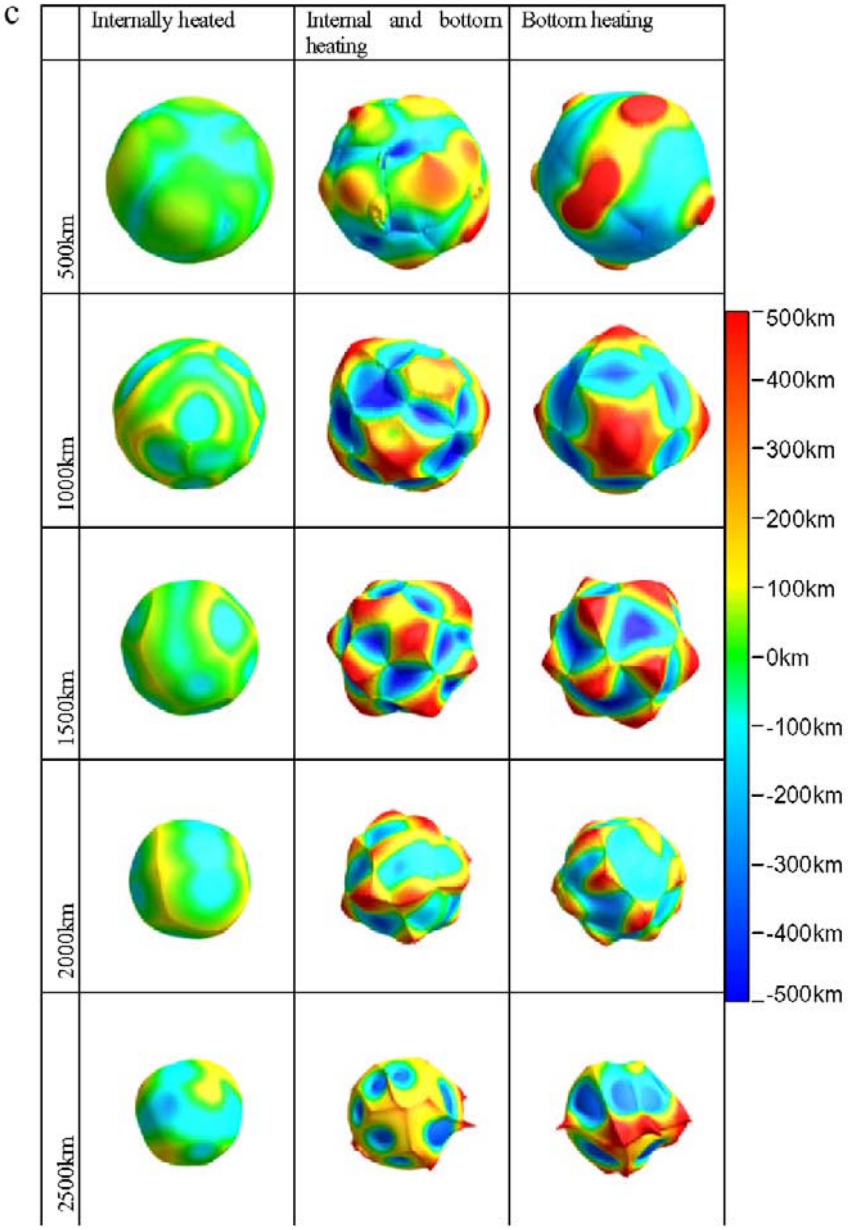

Figure 4. (continued)

caused by different temperature gradients across the CMB. The size of the temperature gradient was determined by the temperature of the lower layer; the hotter the lower layer the less heat was conducted into it since the temperature of the CMB was fixed at 3000 K. The greater temperature contrast for deeper layers can be explained by considering the surface area of the layer. Since heat can only leave the lower layer by conduction then the larger the surface-area of the interface the smaller the temperature contrast across it needs to be to transport the same heat. For a deeper layer the surface area is smaller and so a larger temperature contrast is needed. The increase in the temperature contrast with the chemical density contrast across the deformable boundary is explained by considering that less-dense layers have undulations with larger amplitudes and hence a greater surface area over which they can conduct heat. This is complicated further by the fact that the amount of heat entering the lower layer is not the same for all cases. Since the temperature of the CMB and the surface are fixed, the system must thermally balance itself by arranging values of the average temperature in the upper and lower layers such that the heat flux across all three boundaries is equal. This can only be achieved in certain cases by having negative temperature gradients in the two layers.

[26] For cases where the layer is placed deep in the mantle at a depth of 2500 km the distortions of the interface are so large that sections of the boundary are pressed against the CMB. As a result some heat flux from the CMB is transferred directly to the upper layer. Consequently the temperature contrast across the two layers is not as large as one would expect from extrapolating results in the midmantle. Likewise in cases where the layer is placed in the upper-mantle (500 km depth) undulations can press sections of the interface against the surface resulting in a colder upper layer and very high heat flow at these surface regions.

[27] For the internally heated cases internal heating was active in both the upper and lower layer and so the total heat generated in the system was constant at 2.032×10^{12} W. However, heat generated in the lower layer ranged between 0.14×10^{12} W and 1.50×10^{12} W, depending on the volume, controlled by the depth at which the interface is centered. The amplitude of interface undulations was relatively small for these cases. The lower layer had little to no lateral thermal heterogeneities. This is presumably caused by the lack of a thermal boundary at the CMB that could help drive convection in the lower layer, and possibly subcritical conditions for a few cases. The topography of the deformable boundary was dictated by the presence of cold material from above. Altering only the density contrast had little effect on the temperature contrast across the interface. There is little change in the amplitude of the undulations and so likewise there is little effect on the surface area to cause a change in the size of the thermal gradient. When the interface was placed deep in the mantle the lower layer had a smaller volume and so less heat was generated in it relative to cases where the interface was higher in the mantle. This is reflected in the fact that deeper interfaces require a smaller thermal contrast across the deformable boundary.

[28] Total heat entering the cases where both internal and bottom heating were active ranged from 3.144×10^{12} W to 4.059×10^{12} W. The contribution from bottom-heating to the total heat entering the system was between 36% and 50%. Heat flux into the lower layer ranged between 1.26×10^{12} W to 3.53×10^{12} W with the contribution from bottom heating to the lower layer being between 43% and 89%. For some cases when the boundary depth was set to 500 km or 2500 km distortions of the interface reached the surface or CMB respectively. The temperature contrast over the deformable interface was largest for shallower cases with larger density contrasts. Both the values of the temperature contrast and the way in which they vary with depth resembled those seen in the bottom-heated cases rather than the internally heated cases.

[29] Cutaways displaying the thermal structure of several different cases can be seen in Figures 4a–4c. In Figure 4b the average radial temperature has been removed so the resulting images display the lateral temperature heterogeneities. Significantly lower amplitude thermal heterogeneities are seen in the internally heated cases. These also show very little temperature variance in the lower layer and the amplitude of thermal heterogeneities is larger in the upper layer. The wavelength of the thermal heterogeneities and the size of the convection cells in the upper layer are frequently coupled to the depth of the layer; with the width and the depth of the cells being roughly equal. This can be seen in Figure 4b for the cases where the interface was centered at 1000 and 1500 km depths in particular. In contrast the bottom-heated cases and those with both bottom and internal heating have larger lateral thermal anomalies in the lower layer. The heterogeneities in the upper layer were also larger than those in the internally heated cases.

[30] The temperature power spectrum, calculated following *Bunge et al.* [1997], is shown in Figure 5a. This is a spherical harmonic analysis of the lateral variations in temperature for all depths in the mantle. In all cases the peak of the power spectrum is at the depth of the deformable interface rather than either the surface or CMB. The amplitude of the surface heterogeneities is only comparable to that of the interface in internally heated simulations.

[31] The power spectrum of the amplitude of the deformable boundary was also calculated in the same manner as the thermal power spectrum. See Figure 5b. There is a close relation between the amplitude-power-spectrum and the thermal-power-spectrum. Where dual or triple peaks are present in one, they are also present in the other. The thermal maximum is often of a higher order than the amplitude maximum, suggesting more complex thermal structure; for example, some domes on the interface might be fed by several thermal upwellings.

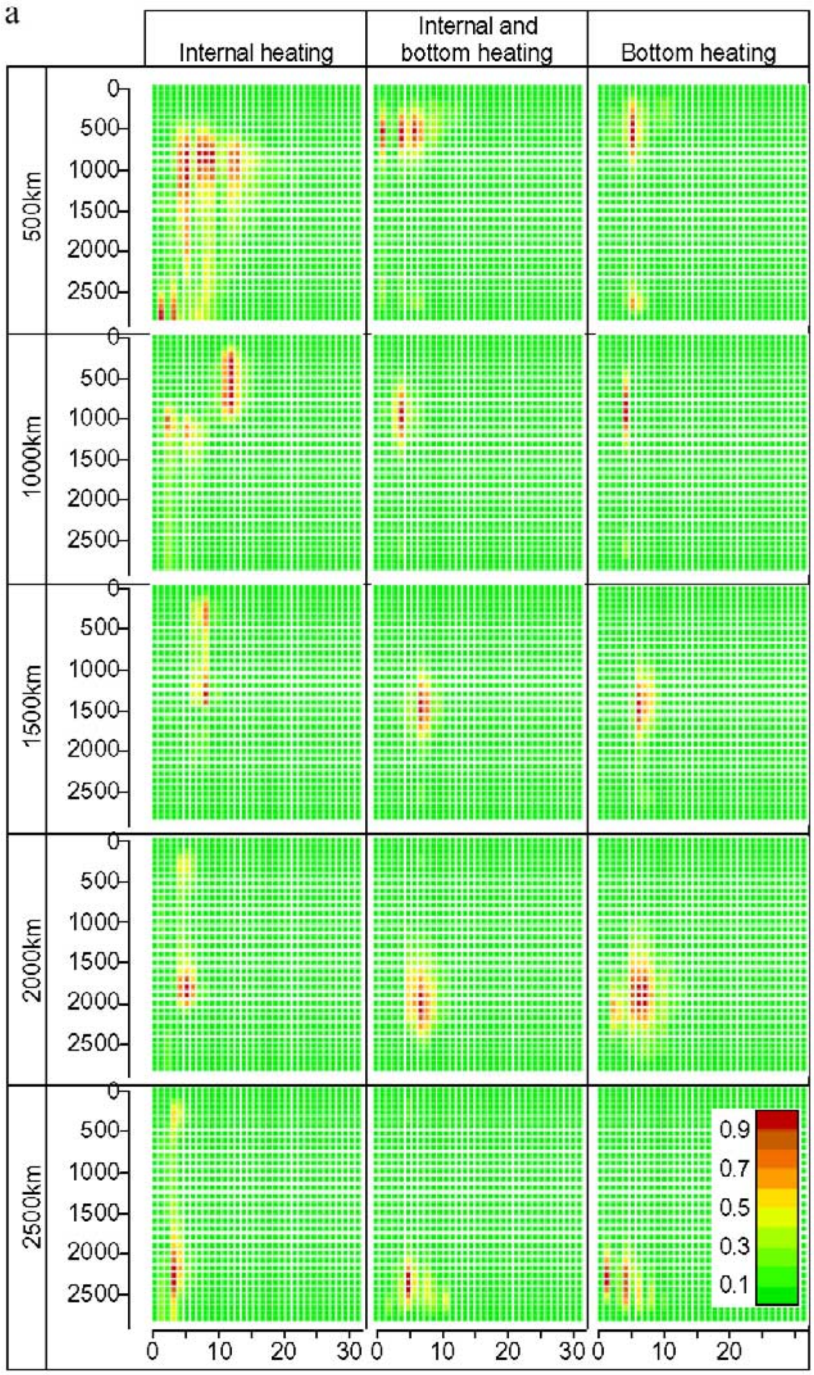

Figure 5. (a) Spherical harmonic contour plots of the thermal field output of the 4% runs for all three heating modes. The x axis is the harmonic degree, while the y axis is the depth in kilometers. (b) Graphs of the spherical harmonic decomposition of the topography of the interface for various cases. The x axis is the harmonic degree, and the y axis is the normalized power in that degree.

[32] The effective density contrast over the boundary can be defined as the chemical density contrast minus that due to thermal expansion:

$$\Delta\rho_{\mathrm{eff}} = ((\rho_1 - \rho_0)) \div \rho_0) - \alpha\Delta T_K, \qquad (2)$$

where $(\Delta\rho)_{\mathrm{eff}}$ is the effective density contrast, ρ_0 and ρ_1 are the chemical reference densities in the upper and lower layers respectively, α is the volume coefficient of thermal expansion, ΔT_K is the temperature contrast associated with the thermal boundary as illustrated in Figure 2.

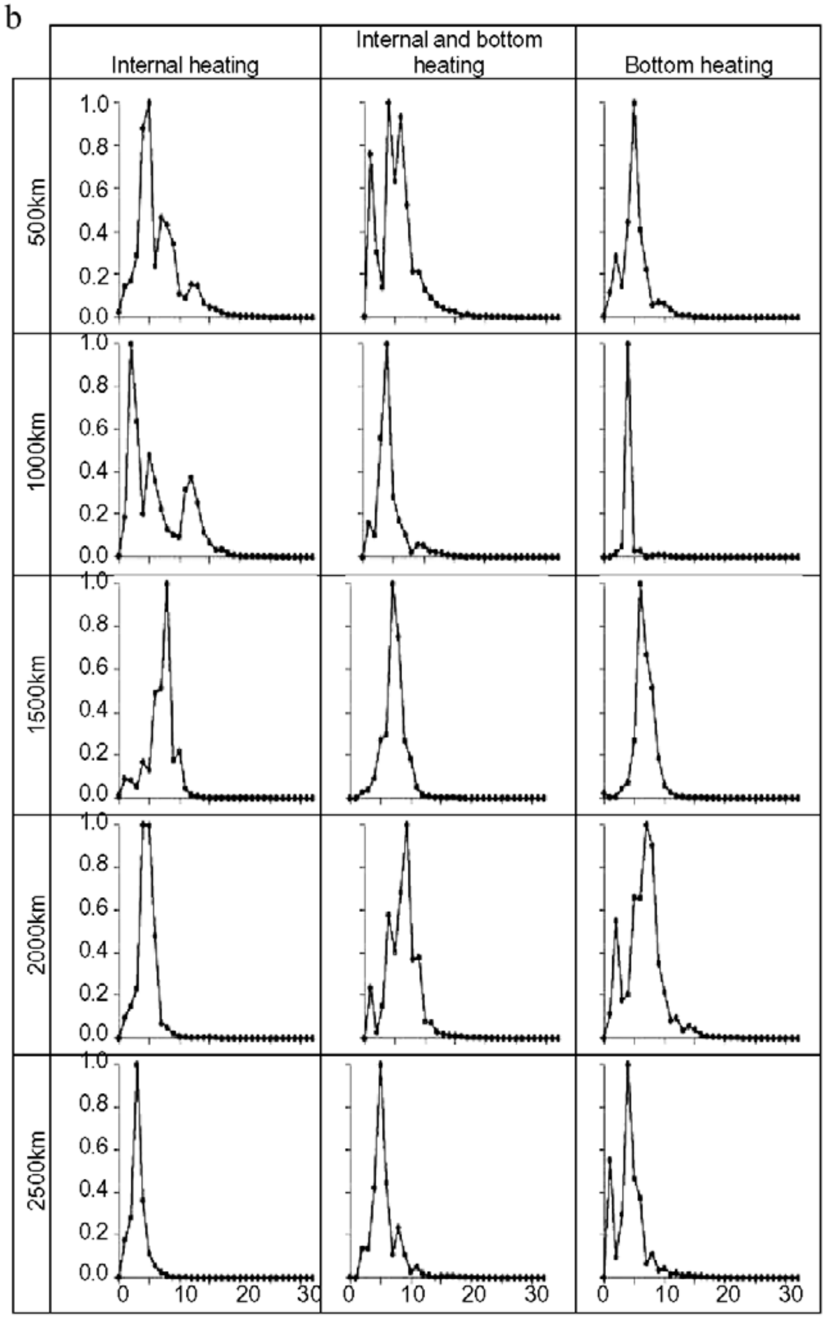

Figure 5. (continued)

[33] The effective density contrast for all the stable steady states is illustrated in Figure 6. The small temperature contrast needed in the internally heated cases (shown in Figure 6) suggests that the contribution of thermal expansion does not significantly change the density contrast over the layer. This is due to the relatively low heat energy that is being inputted into the lower layer in the internally heated cases, rather than the heat mode itself. For internally heated cases and cases with both internal and bottom heating the shallower and less dense interfaces had the smallest effective density. In bottom-heated cases the effective density contrast is smallest in deep layers with a small density increase across the deformable interface.

[34] Once the layered system has reached a quasi-steady state it is in quasi-thermal equilibrium.

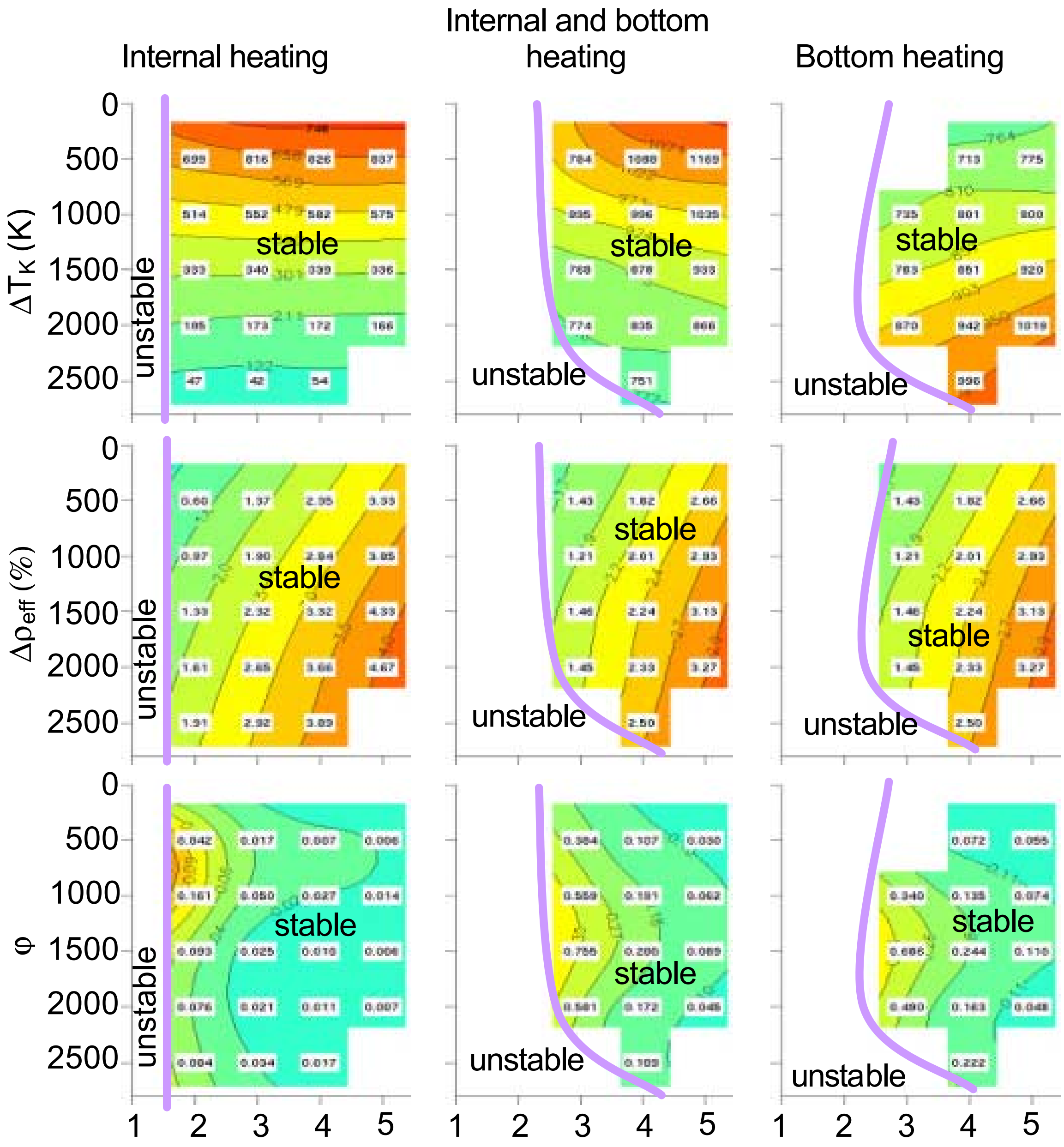

Figure 6. Contour plots showing how several physical characteristics of the layered systems alter with the depth of the boundary and the density contrast across it. The density contrast is shown on the x axis, and the depth of the boundary is shown on the y axis. The temperature in the upper and lower layers is defined as the average temperature halfway between the deformable interface and either the surface or the CMB. The temperature contrast used here is the difference between these two values. The effective density contrast is the chemical density contrast minus that due to thermal expansion and is defined in equation (2). The Nondimensional Area Variable φ is the fractional increase in the surface area of the interface relative to the area of a shell at the same depth as the interface. So $\varphi = 0$ implies a flat layer and increasing values of φ represent a more deformed boundary. The purple line shows where the regime changes from stable to unstable.

Therefore heat energy entering the lower layer either through internal heating (radioactive decay, secular cooling) or from bottom heating (conduction over the CMB) must then be balanced by heat leaving the lower layer by conduction over the deformable boundary (see Figure 1). This conductive heat flow is described by

$$Q = -kA\frac{dT}{dz}, \tag{3}$$

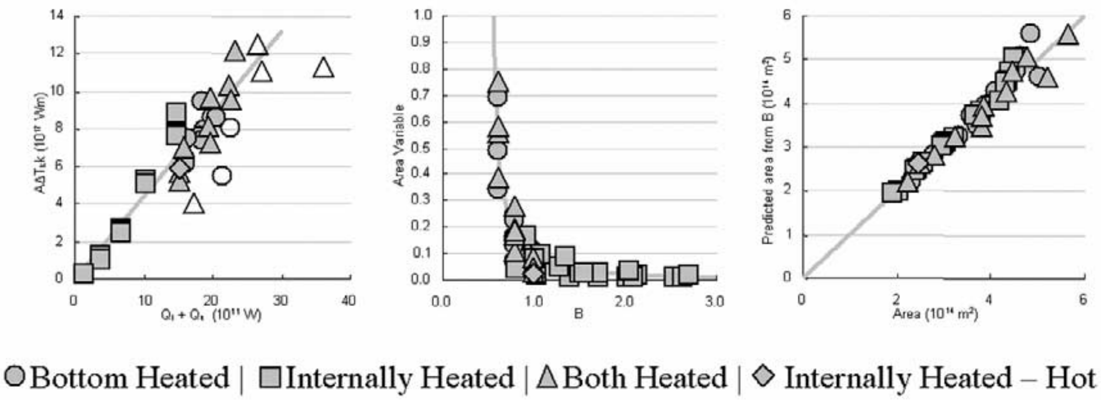

Figure 7. Each symbol represents the result of one simulation. Unfilled symbols represent cases where the deformable boundary pushes against either the CMB or the surface. (a) Heat balance in the lower layer. A plot of the total heat energy in the lower layer against $kA\Delta T_K$. The gradient represents the size of the thermal boundary ΔZ. The gray line displays the best fit that corresponds to a ΔZ of 437 km. The results for all the heat modes are displayed, and we see that these all plot well as a straight line, suggesting there is little variance in the thermal structure caused by the heating mode. (b) The relationship between the nondimensional area variable and the buoyancy ratio. The gray line represents $B = 0.07 \div (B^2 - 0.48^2)$. (c) A plot of the predicted surface area of the deformable boundary using the buoyancy values against the observed areas.

which can be approximated by

$$Q = -kA\frac{\Delta T_K}{\Delta Z}, \qquad (4)$$

where Q is the total heat flow, k is the thermal conductivity, A is the surface area over which heat energy is being transported by the conduction, ΔT_K the temperature difference across both thermal boundaries associated with the interface between the layers, and ΔZ is the thickness of both thermal boundaries (see Figure 2).

[35] Figure 7a shows the heat flow (Q) against $kA\Delta T_K$ which should plot as a straight line assuming that the thickness of the thermal boundary is the same for all cases and unaffected by the type of heating mode being used. The straight line plotted through would suggest a thickness of interfacial boundary layers of ~440 km. The thermal structure of the layered system is found to be largely independent of the heating mode being used. Only heat balance considerations need to be used to explain the thermal structure of the layered systems and the thermal boundaries associated with them.

[36] To describe the size of the deformation of the deformable boundary, we define the following nondimensional area variable φ:

$$\varphi = \frac{A - A_0}{A_0}, \qquad (5)$$

where A is the surface area of the interface between the two layers and A_0 is the surface area of a shell at the same radius (r) as the interface ($A_0 = 4\pi r^2$), i.e., the area of the undeformed interface.

[37] The relationship between B and φ is shown in Figure 7b. It is possible to fit the data with the following relationship:

$$\varphi = \frac{a}{B^2 - b^2}. \qquad (6)$$

Using least squares, the constants a and b are found to have values 0.07 and 0.48 respectively. The value of b corresponds to the buoyancy ratio B when the nondimensional area variable tends to infinity. This would suggest that the layered system is unstable when the buoyancy ratio is less than 0.48. Unfortunately the span of data points is insufficient to tightly constrain either the form of equation (6) or the parameter values for applications involving extrapolation. Therefore for such cases, there is a large error in this value of b. Within the region where we have experimented, i.e., for interpolation, the expression works well. For example equations (5) and (6) can be combined to predict the surface area of the deformable boundary for each case using the buoyancy ratio. The good match can be seen in Figure 7c. The relationship between the size of the deformation of the layer's interface and the buoyancy ratio is largely unaffected by the type of heating mode present in the layered system. We also note that the absolute values of φ is not well constrained since it varies with the resolution of the grid used (see Appendix B).

[38] The internally heated cases proved to be more stable than the cases with bottom heating. For cases with internal heating only $\Delta\rho = 2\%$ was sufficient for stratified systems, while for cases with bottom heating $\Delta\rho = 3\%$ or greater was required. However, it was not clear if this was because of the heating mode or the smaller levels of heat energy in the lower layer. To test the effects of increasing the heat energy in the lower layer, an extra internally heated case was run with the interface centered at 2000 km depth, and an intrinsic density contrast of 5%. The internal heating in the upper layer was turned off and that in the lower layer was increased by a factor of 4. We note that this ''internally heated–hot'' case has a similar ΔT_K to the bottom-heated equivalent case, and similar total energy input to the bottom layer. The ''internally heated–hot'' case has lower interface deformation (marker standard deviation, 70 km versus 104 km; and φ, 0.020 versus 0.048, Table 2). The temperature in the upper and lower layers is very similar in both cases. Therefore the results of this calculation suggest that the internally heated cases are at least as stable as the equivalent bottom-heated cases. The results of this ''internally heated–hot'' case are shown in Figure 7, and the results of all the experiments are summarized in Table 2.

4. Discussion

[39] One prominent feature that these models demonstrate is the increased temperature of the lower layer, as found in previous work on layered systems (see ΔT_K in Table 2). The heat from the lower layer needs to be conducted across the boundary and therefore a double thermal boundary must develop. Therefore guided by the temperature drop across the surface boundary layer (e.g., oceanic lithosphere) one might expect temperatures around a thousand degrees hotter in the lower most mantle for an actual layered case than in equivalent whole mantle convection. At the lower Rayleigh number of our simulations we find weaker thermal boundary layers, varying from $\sim$50 to 1200 K. The increase in temperature in the lowermost mantle is observed clearly in all models in Figures 4a–4c with bottom heating. Such a hotter lower mantle clearly has many implications, including for radial seismic models and for thermal evolution models. For example, layering causes the body to cool slower, and hence today's heat flow will have a higher contribution from secular cooling, and the thermal structure will be more sensitive to the initial temperature [*Richter and McKenzie*, 1981].

[40] It is important to remember that due to approximations the system we have modeled is not Earth or any other planet. Differences include minor assumptions such as the Boussinesq approximation and fluid incompressibility, and more important simplifications such as the constant viscosity, thermal conductivity and coefficient of thermal expansion. Also the vigor of convection was weaker in our models than estimated for Earth's mantle, and plate tectonics of Earth's surface is not simulated. While it is misleading to talk in terms of a single Rayleigh number when comparing internally heated and bottom-heated systems it can probably be said that Ra of these cases is around 2–3 orders of magnitude smaller than Earth's mantle.

[41] For a layered system in which heat is being transported across the interface between the layers solely by conduction we have shown that the heat balance of the lower layer can be used to explain the thermal structure of the system. In our simulations, while it can take 100 billion years for the bottom layer to adjust its temperature for the system to be in a quasi steady state (see Figure 3), we note that since the RMS surface velocities in our calculations were from 6×10^{-3} to 7×10^{-2} cm/yr, compared to 5 cm/yr observed today; this implies that 100 Gyr model time is more like 0.1–1.2 Gyr for Earth. Therefore one could expect a layered system to approach quasi-steady state in 4.5 Gyr (though for Earth it would never quite get there since it would be tracking a declining rather than steady internal heat generation rate).

[42] We note that the work of *Castle and van der Hilst* [2003a, 2003b] and *Vidale et al.* [2001] did not detect any sharp global reflector (<20 km width) between a depth of 800 and 2000 km. They suggest that they could detect reflections from interfaces with velocity differences of greater than 2%, and topographic interface gradients of less than some 30 degrees. It is possible that the changes in composition and thermal structure combine such as to minimize the impedance contrast (the change that leads to reflections). If so, it is highly unlikely to be able to also hide the larger seismic volumetric signal that the much broader thermal boundary layers should present, as discussed by *Tackley* [2002]. Such a signal is not seen between 800 and 2500 km in seismic tomography studies. We note that for cases where this is investigated the proportion of the interface with slopes less than 30 degrees varies with B from 30% at low B to 90% when B is 2 [*Oldham*, 2004]. While significant topography is found on the interface in our simulations, it is not as great as

30 degrees. The penetration of subducting slabs through the uppermost lower mantle, as well evidenced in the work of *van der Hilst et al.* [1997] and *Grand et al.* [1997], argues strongly against a layer in the shallower lower mantle. It is though more difficult to currently rule out the presence of a layer in the deeper most mantle. There are many possibilities including D″, and megapiles.

[43] While as discussed above this work is preliminary in how it relates to present-day Earth, it suggests that maybe intrinsic density contrasts of 2–3% or greater can lead to stability. The observed density contrast across the layer is reduced from the higher intrinsic density contrast since the lower layer is hotter; but as can be seen from Table 2, one could still expect observed density contrasts of order a few percent, and relatively small interface topography. Since the expected topography is small, the density contrast would not be smeared out over a great depth interval and therefore the sharp increase might be resolvable in radial seismic models. We note that the lower mantle radial density gradient in PREM [*Dziewonski and Anderson*, 1981] is ~1% increase in density per 100 km increase in depth. No radial seismic models have recorded a global density discontinuity in the lower mantle. It is possible that this arises from the assumptions sometimes applied, e.g., that the Adams-Williamson equation applies in the lower mantle, as in PREM. We do note that *Ishii and Tromp* [1999, 2001] argue that they have detected a lateral RMS density variation in the lowermost mantle of up to 0.4% by tomography, with a correlation between regions of increased density and reduced shear velocity close to the CMB. This is controversial [see *Kuo and Romanowicz*, 2002; *Resovsky and Ritzwoller*, 1999]. The work of *Resovsky and Trampert* [2002] finds the RMS error bars on lateral density variations vary from 0.35% to 0.6% through the lower mantle. *Bina* [1998] argues that observations limit the radial density differences to less than 2%. This is based on the work of *Montagner and Kennett* [1996], who did not constrain the form of the density variation with depth. This largest density variation was detected in the deepest and shallowest lower mantle. Our results, which are suggestive of needing density contrasts of greater than 2% for long-term stability, therefore suggest that chemically stratified mantle convection is unlikely unless combined with layering induced by an endothermic 660 km discontinuity. The velocity contrasts would be expected to be even greater than the density contrasts, and again in radial seismic models there is no unequivocal recorded global seismic velocity discontinuity in the lower mantle, above D″. While *Deuss and Woodhouse* [2002] find no evidence for global lower mantle discontinuities, *Vinnik et al.* [2001] argue for global discontinuities at ~900 km, ~1200 km, and ~1700 km depth.

[44] Using the work of *Forte et al.* [2002], density contrasts of order 3% would require changes in molar fraction of iron of order 10% and changes of order 100% in mole fraction of perovskite. These are large variations and might be expected to have implications on the seismic velocity structure, in addition to the density structure. Since the effect of iron on velocity is opposite to that of perovskite, it might be possible to limit the variations in seismic velocity structure by having both variations. The change in molar fraction of perovskite could result from varying silica content of the layers.

[45] Recent imaging of the deep mantle has revealed two large slow anomalies in the deep mantle [*Wei-Jia and Dziewonski*, 1991; *van der Hilst et al.*, 1997]. A thermal anomaly alone is not thought to be sufficient to generate these features [*Forte and Mitrovica*, 2001]. It is speculated that there must be some compositional contribution to their seismic structure. These anomalies are dome shaped and often referred to as ‘‘megaplumes’’ [*Matyska et al.*, 1994]. It has been speculated that these megaplumes structures are responsible for superswells, areas of Earth’s surface that contain a high density of hot spots [*Courtillot et al.*, 2003]. Superswells are observed in eastern Africa and Polynesia; both are directly above the seismically observed megaplumes. Plumes rising from above these chemically distinct reservoirs could be enriched by the reservoir and so have a different chemical structure to plumes from other sources. This could, it is claimed, explain the variation in plume geochemistry [*Courtillot et al.*, 2003]. Evidence that the mantle below superswells is chemically enriched [*Janney et al.*, 2000] could further support leakage from a primitive megaplume.

[46] We note in our results that when the interface is in the deeper most mantle the spectral character of the thermal and interface structure become longer wavelength, lower harmonic degree, approaching l = 2 for the bottom-heated case, increasing to l = 3 to 5, for cases with internal heating (Figures 5a–5b). If this trend toward longer wavelength is enhanced by more realistic conditions then it is possible that the ‘‘megaplumes’’ could reflect a deep layer with extreme

topography. We note that *Forte et al.* [2002] argue that while these features have a different chemistry they are flowing upward, suggesting that the thermal buoyancy is overcoming the intrinsic chemical buoyancy and that they might not form distinct layers. The associated observation in our numerical experiments that the interfacial features are very stable could be related to the relative fixity of hot spots if we assume that they are generated by mantle plumes rooted on upwelling cusps in the interface. This type of behavior has also been found in laboratory experiments simulating a chemical layer in D″ [*Jellinek and Manga*, 2002; *Davaille et al.*, 2002].

[47] We note that this generic work will also be of value in understanding the character of chemically stratified convection in other planetary mantles. For better application to Earth this work needs to be extended to higher Rayleigh number with more realistic material properties.

5. Conclusions

[48] The simulations of stratified convection for three heating modes; with the interface centered at a range of depths from 500–2500 km, have been undertaken for a range of intrinsic density contrasts. Density contrasts from 2 to 4% were required to produce layering which are slightly greater than current estimates of plausible intrinsic density contrasts [*Bina*, 1998]. The introduction of a stable chemical layer into a 3-D spherical system produces a large two-sided thermal boundary at the interface. For cases with bottom heating the lower layer becomes very hot. Thermal expansion of the lower layer can reduce its density contrast and aid its invisibility to seismic imaging. However, the thermal power spectrum shows peaks, centered on the interface, that are inconsistent with the results of seismic velocity tomography.

[49] Therefore while we note that the current simulations are not at Earth like vigor and lack realistic spatial (lateral and radial) variations in certain key properties, the current simulations, combined with the lack of evidence for seismic reflections [*Castle and van der Hilst*, 2003a, 2003b; *Vidale et al.*, 2001; *Deuss and Woodhouse*, 2002] tend to argue against layering between 500 and 2500 km depth. The more likely scenario for a stable chemical layer is either a very shallow (e.g., continental lithosphere, which we have not discussed or addressed) or a very deep layer (D″, piles, etc). Here large sections might be, of the order of, or thinner than, the size of the thermal boundary at the CMB/surface. We also note that the interfacial features are slow moving compared to features on the top boundary. This suggests a possible mechanism for the fixity of hot spots, if they were generated by plumes rooted at such an interface [*Davaille et al.*, 2002; *Jellinek and Manga*, 2002].

Appendix A: Method

[50] We have developed a method to simulate mantle convection in a layered three-dimensional (3-D) spherical system by adapting the well-established TERRA code [*Baumgardner*, 1985; *Bunge and Baumgardner*, 1995]. TERRA solves the equations for the conservation of mass, conservation of momentum and conservation of energy; for infinite Prandtl number creeping viscous flow and marches the solution forward in time using a second order Runge-Kutta scheme. It uses a finite element discretization, and solves the system of equations for the velocity using a multigrid algorithm. The code has been parallelized and is run on Beowulf computing clusters.

Mass
$$\nabla \cdot \underline{v} = 0, \tag{A1}$$

Momentum
$$\frac{1}{\rho} \nabla P = \nu \nabla^2 \underline{v} - \alpha g \Delta T, \tag{A2}$$

Energy
$$\frac{\partial T}{\partial t} + \underline{v} \cdot \nabla T = \kappa \nabla^2 T + \frac{J}{\rho C_P}. \tag{A3}$$

The chemical boundary is represented by an array of markers. Each marker is defined by its coordinates in space (x_1, x_2, x_3) the positions of which are updated using a Runge-Kutta time step.

$$x_{i_{t+\Delta t}} = x_{i_t} + v_{i_{t+\frac{1}{2}\Delta t}}\left(x_{i_{t+\frac{1}{2}\Delta t}}\right)\Delta t, \tag{A4}$$

where x_i i = 1, 2, 3 is the markers' coordinates, v_i the velocity and Δt the size of the time step.

[51] The velocities used are interpolated from the solved velocities at the nodes. TERRA uses an icosahedral grid [*Baumgardner*, 1985] and hence each marker is located within a triangular prism defined by six nodes. See Figure A1a. The velocity of each marker is interpolated from the velocity of surrounding six nodes by taking a weighted mean.

[52] The icosahedral grid is divided up into radial spokes running from the CMB to the surface. Each spoke owns a stretched hexagonal volume (see

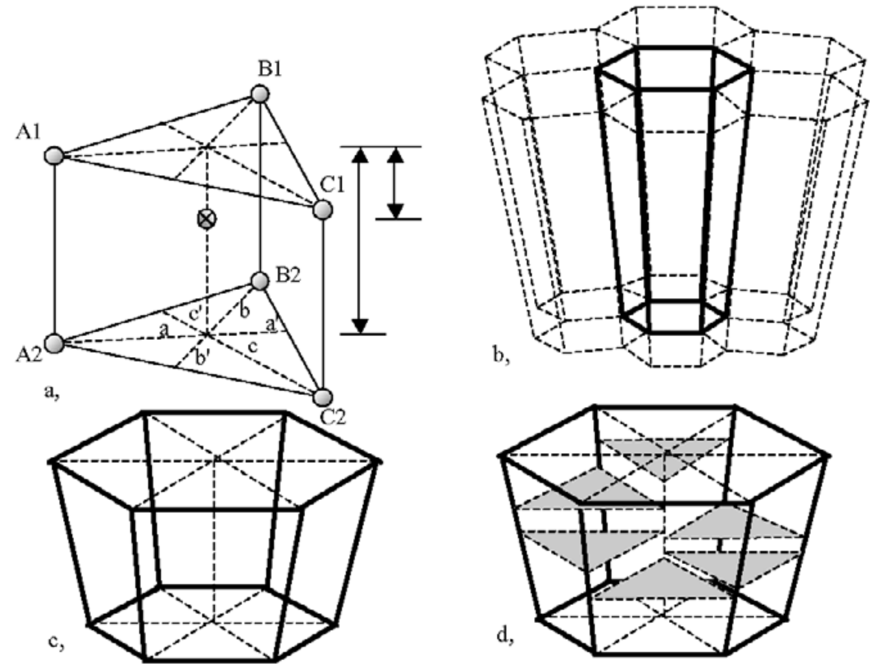

Figure A1. (a) The lengths a, a′, b, b′, c, and c′ are used to calculate the weighting to interpolate properties of markers from the six surrounding nodes. (b) The stretched hexagonal volumes of the icosahedron grid. Each "spoke" contains 6 to 12 markers. (c) The decomposition of each spoke into six prisms. Each prism contains at least one marker. (d) An example of the method used to find the ratio of the upper and lower layer volumes associated with each node. The hexagonal region "owned" by the nodes is divided into six triangular prisms. The average height of the markers present in each prism is used to divide the prism into two. The sums of the appropriate individual prism volumes are used to give the total volumes associated with each layer and hence the ratio of the two.

Figure A1b). After each time step each marker's new position is used to see if it has moved into a new spoke. The size of the time step is limited such that a marker can only move at most to a neighboring spoke. The number of markers in each spoke is variable with a minimum value of 6 and a maximum of 12. If the number of markers in a spoke has fallen outside of this range then markers are either destroyed or created in the manner described below.

[53] To reliably calculate buoyancy forces, it is necessary to find the ratio of the volume of the upper and lower layers associated with each node. To do this, the distribution of markers has to be evenly spread out within a hexagonal spoke. Each spoke is divided into six stretched triangular prisms. See Figure A1c. After each time step in the Runge-Kutta scheme each triangular prism is checked to see if it contains at least one marker. If there is no marker in the prism a new one is created. This is done by projecting a plane through three existing (with good azimuthal spread) markers and placing the new marker at the intersection of this plane and the centre of the triangular prism. In the event of a spoke containing more than 12 markers; markers are then randomly selected for deletion such that each prism will still contain a marker. This method of creating and destroying markers ensures that the spatial resolution of the marker surface is always higher than the resolution of nodes in the TERRA grid.

[54] The density contrast ($\Delta\rho$) associated with the boundary is introduced in the buoyancy term of the force equation:

$$\frac{1}{\rho}\nabla \mathrm{P} = \upsilon\nabla^2 \mathrm{v} - \mathrm{g}\left(\alpha\Delta \mathrm{T} + \frac{\Delta\rho}{\rho}\right), \tag{A5}$$

where P is the nonlithostatic pressure, ρ is the density, ν is the kinematic viscosity, v is the velocity, g is the gravitational force per unit mass, α is the coefficient of thermal expansion and ΔT is the temperature anomaly relative to the radial reference temperature profile.

[55] The contribution of the density at each node is defined by the position of the node relative to markers i.e., whether the node is above or below the boundary. This process has been described as

rasterization by *Schmalzl and Loddoch* [2003]. For nodes whose volume contains one or more markers the density is taken to be the average of the densities in the two layers weighted by the volume of each layer associated with the node. The volume ratio is found by subdividing the hexagonal volume horizontally into a series of triangular prisms. The average height of the markers in each prism is then used to calculate the volume of each layer within the prism. This is then repeated for all six prisms and the results are summed to give the volume of the upper and lower layer associated with the node. See Figure A1d.

[56] Tank experiments using miscible fluids show entrainment of fluid from one layer into the other layer even when the systems are well stratified [e.g., *Davaille*, 1999a]. Numerical experiments in contrast have frequently not allowed, or tried modeling this entrainment [*Kellogg et al.*, 1999]. We estimate the amount of entrainment one can expect using the work of *Gonnermann et al.* [2002], who extend the work of *Davaille* [1999a, 1999b]. They predict the rate of entrainment Q (m^3/m^2 per s; upward and downward) as

$$Q = k\frac{CH^{-1}B^{-2}Ra^{1/3}}{1 + \gamma B^{-1}}, \tag{A6}$$

where C is an experimentally derived constant, for $B > 0.2$ $C = 0.2$ [*Davaille*, 1999b], κ is thermal diffusivity, H is the total fluid depth, B is the buoyancy ratio as defined by *Davaille* [1999a] (see equation (1)), Ra is the Rayleigh number and γ is the ratio of the upper layer viscosity to the lower layer viscosity (equal to one in our calculations).

[57] For the mantle, *Gonnermann et al.* [2002] show that the rate of entrainment for the mantle with a buoyancy ratio of around 1 would be very low, such that the system could approach a thermal steady state. From applying the above formula to our simulations (e.g., $\Delta\rho = 2\%$) we find the expected rate of entrainment can be quite high, such that the layering would change at a faster rate than the system would approach thermal steady state. Therefore we have limited entrainment in our calculations using a rescaling filter so that they better simulate the expected Earth behavior (if the mantle is layered). In the rescaling filter the marker's heights are periodically rescaled to remove the effects of entrainment.

[58] While our marker method reliably models a layered spherical system, it is limited to stratified cases. It is unable to model a system in which the sides of the markers' boundaries approach the near vertical. The marker method could be extended to cope with extreme deformations of the interface by using a more sophisticated method such as the front tracking method of *Schmalzl and Loddoch* [2003]. This would increase the applicability of the code, but is not required for modeling our target cases of stratified systems.

Appendix B

[59] A number of verification tests were performed on the marker method used in the simulations presented here. The velocity of the markers is found by interpolating the values of the velocity at the surrounding nodes. The method used to interpolate these velocities was tested by applying an artificial velocity field that moved the markers radially. This had the advantage that markers would not move into new elements and so the marker population controls were not used. The error in the markers position after they have been advected for 14,000 km is found to be 0.1%.

[60] The population control of the markers is tested by applying an artificial velocity field that rotates markers around the pole. As markers are moved from element to element population controls are used to create and destroy markers. Markers are initiated as a flat spherical shell and so should remain as a shell if the population controls are efficient. After the markers have been rotated 12 times (i.e., a total distance of 367,000 km) the average height of the markers had fallen by only 28.8 km and the root mean squared (RMS) heights of the markers had increased to 29.2 km. If the RMS heights of the markers are representative of the contributions of marker population controls to the error in moving the markers then an error of 0.0079% is collected over 4000 iterations.

[61] Tests were run in which the time step was varied. This was found to have a negligible effect on the output of the simulations.

[62] A resolution test was run with coarse grid (1,310,720 nodes, a data point every 100 km) and a fine grid (10,485,760 nodes, a data point every 50 km). The systems had both bottom and internal heating. The viscosity structure within the system varied with depth. Parameters used can be seen in Table B1.

[63] The initial condition used in both simulations was identical with the higher-resolution initial case being interpolated linearly from the lower order

Table B1. Parameters Used in the Resolution Test

Parameter	Variable	Value
Depth of marker surface	D_k	1500 km
Temperature of surface	T_S	1060 K
Temperature of CMB	T_{CMB}	3000 K
ρ upper layer	ρ_0	5.00×10^3 kg
ρ lower layer	ρ_1	5.20×10^3 kg
$\Delta\rho/\rho$		4%
Dynamic viscosity η	η	4.000×10^{23} Pa s (with radial layering)
Rate of internal heating	Q_{rad}	4.50×10^{-12} W kg^{-1}
Volume coefficient of thermal expansion	α	2.0×10^{-5} K^{-1}
Specific heat at constant volume	C_V	1×10^3 J kg^{-1} K^{-1}
Rayleigh number	Ra	8.4×10^4

case. The coarse and fine simulations were run for 77.278 billion years; this corresponds to 17 over turns of the system. Figure B1 shows cross-section images of the two cases at the end of the runs. The two final cases are similar, but not identical. The planform of upwelling features in the lower layer is similar in both case and this figure does not suggest that the lower resolution case might be unresolved. A more detailed description of the state of the two simulations is shown in Table B2. This compares a series of parameters outputted during the simulations. These all agree to within one percent and suggest that the system is resolved, (with the exception of the area parameter see below). The variation of the thermal structure and the Nusselt number with time show good agreement; see Figure B2. However, the nondimensional area variable is consistently larger in the cases with a higher grid resolution. We suggest that this discrepancy is caused by using a different scale to measure the surface area. If this is the case then the fine grid space simulation's surface area is around 1.3 times that of the coarse grid space simulation's surface area.

[64] The radial rescaling filter used to compensate for the effects of entrainment is tested to see if it has an effect on the properties of the layer once it has reached a thermally balanced system. A layered simulation was run starting from an initial case that was not layered. This system was allowed to work toward a quasi-steady state with the radial rescaling filter. During this filtering was employed and around 41 G years were simulated with the rescaling filter. The simulation was then allowed to continue with the filter turned off for a further 15 G years. This final stage of the simulation was repeated but with the filtering on. The results of these models can be seen in Figure B3. The variation between the filtered and unfiltered cases

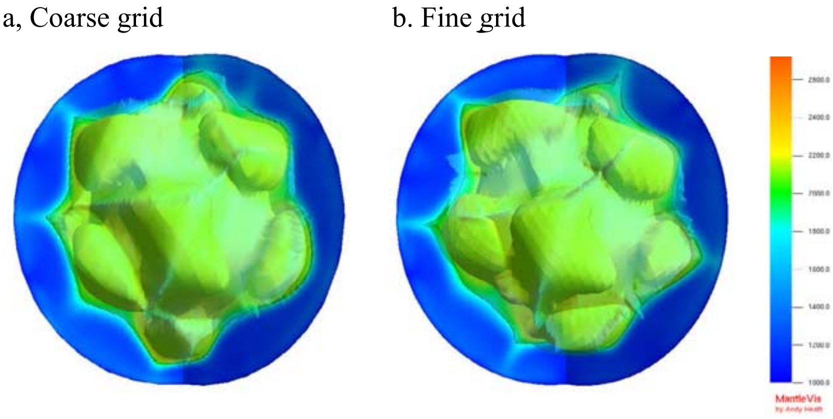
a, Coarse grid

b. Fine grid

Figure B1. (a) Coarse grid. (b) Find grid. The same but different. Shown are MantleVis images of the layered structure of identical cases but run with different grid resolutions. The deformable boundary is represented by a semitransparent surface, and an isosurface at 2000 K is shown.

Table B2. Output Parameters of the Convergence Test[a]

Variable	Coarse Grid	Fine Grid	% Difference
Rms surface velocity	0.1219 cm/year	0.1230 cm/year	−0.902%
Mean surface heat flux	0.006313 Wm^{-2}	0.006308 Wm^{-2}	0.079%
Nusselt number	7.089 ± 0.025	7.067 ± 0.022	−0.167%
Area Variable	0.3370 ± 0.0212	0.4262 ± 0.0147	−26.491%
Temperature of upper layer	1275.485 ± 1.010 K	1281.427 ± 1.026 K	−0.466%
Temperature of lower layer	2405.611 ± 2.152 K	2429.268 ± 3.068 K	−0.983%

[a] In cases with errors quoted the value of the parameter is the average value of the parameter in the calculation between 50 and 70 G years in the simulation. The errors quoted are the standard deviation of the parameter during the same period.

in terms of thermal structure is small and is not thought to alter our results once the simulation has reached a quasi steady state.

Notation

ΔT_k	difference between the temperature in the lower and upper layers, K (Figure 2).
ΔT	difference between the temperature of the CMB and the surface.
ρ	density, kg m^{-3}.
B	buoyancy ratio, defined in equation (1).
$\Delta\rho$	intrinsic density increase across the deformable boundary, kgm^{-3}.
α	volume coefficient of thermal expansion K^{-1}.

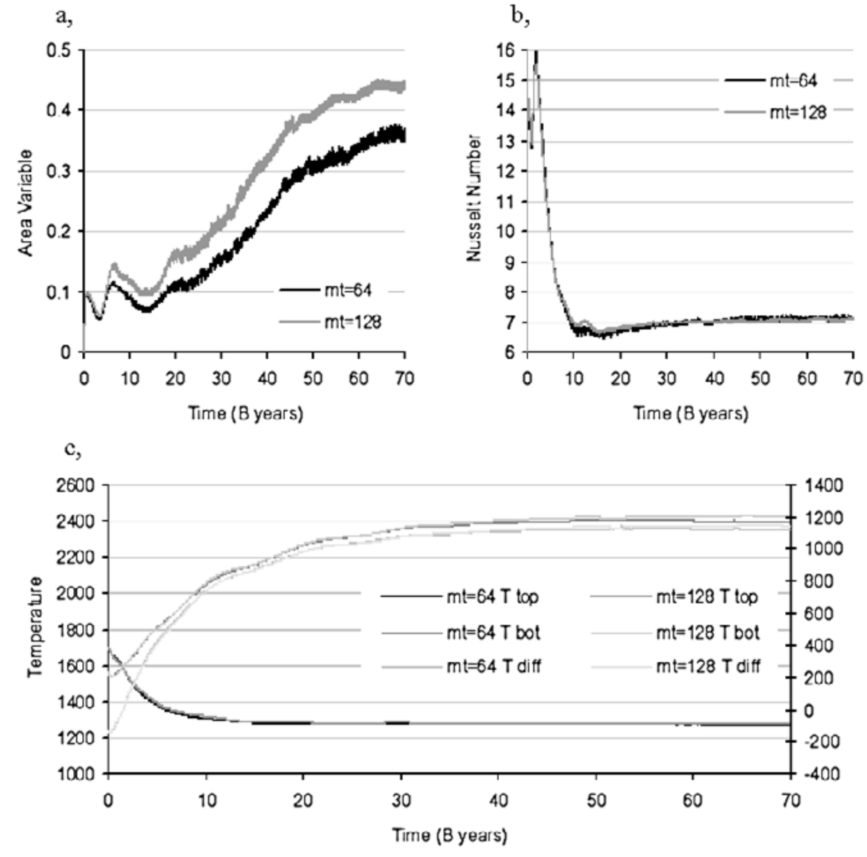

Figure B2. Results from the resolution test. (a) The area of the deformable boundary during the runs at both resolutions. The manner in which the area changes in time is very similar; however, the scale of the area is larger for the cases in which its area is estimated on a higher-resolution scale grid. (b) The Nusselt number of both runs. (c) The thermal structure of runs. T_{top} and T_{bot} are the temperatures of the upper and lower layers, respectively. These are both plotted on the left axis. T_{diff} is the difference between the temperature in the upper and lower layers. It is plotted on the secondary axis on the right.

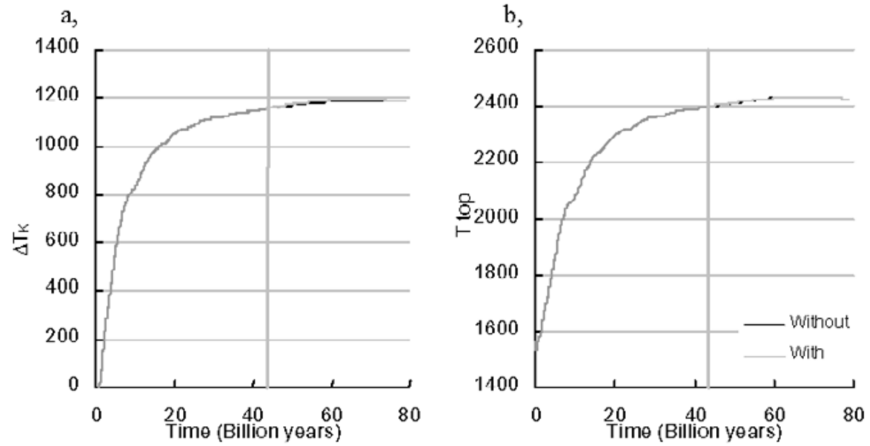

Figure B3. The results of the filtering test. The vertical gray line represents the point at which filtering is turned off.

$(\Delta\rho)_{eff}$	effective density increase across the deformable boundary; chemical density increase minus the effect of thermal expansion; see equation (3); kg m^{-3}.
Q	heat energy, W.
k	thermal conductivity, W m^{-1} K^{-1}.
A	surface area of the deformable boundary, m^2.
A_0	surface area of a spherical shell centered at the same depth as the deformable boundary, m^2.
T	temperature, K.
ΔZ	physical thickness of the thermal boundary associated with the deformable boundary (see Figure 2), m.
φ	nondimensional area variable, defined in equation (6); this is a measure of the increase of the surface area of the deformable boundary from a flat spherical shell; $\varphi = 0$ indicates a flat shell, while $\varphi = 1$ indicates the area has doubled.
a, b	constants used to relate φ to B.
η	dynamic viscosity, Pa s.
g	gravitational acceleration, m s^{-2}.
C_V	specific heat at constant volume, J kg^{-1} K^{-1}.
κ	thermal diffusivity, m^2 s^{-1}.

Acknowledgments

[65] We thank Andy Heath (University of Liverpool) for the development of MantleVis (the parallel visualization tool used to generate Figures 4a–4c), Peter Bunge (Ludwig-Maximilians-University, Munich), and John Baumgardner (Los Alamos) for providing the TERRA source code. D.O. acknowledges the current support of the School of Earth, Ocean and Planetary Sciences at Cardiff University and the earlier support of the Department of Earth Sciences at the University of Liverpool. HEFCE (JREI) supported NESSC, the cluster super computer used to perform most of these calculations. HEFCW (SRIF) partly supported the Helix cluster which was used for some of the calculations. We thank Cinzia Farnetani, Allen McNamara, and Peter van Keken (Associate Editor) for their perceptive reviews that led to improvements in this paper. We also would like to thank the excellent editorial handling of Karen Fischer and the editorial work of Peter van Keken.

References

Allegre, C. (2002), The evolution of mantle mixing, *Philos. Trans. R. Soc. London, Ser. A*, *360*, 2411–2431.

Allegre, C. J., A. Hofmann, and K. O'Nions (1996), The argon constraints on mantle structure, *Geophys. Res. Lett.*, *23*, 3555–3557.

Ballentine, C. J., P. E. van Keken, D. Porcelli, and E. H. Hauri (2002), Numerical models, geochemistry and the zero-paradox noble-gas mantle, *Philos. Trans. R. Soc. London, Ser. A*, *360*, 2611–2631.

Baumgardner, J. R. (1983), A three-dimensional finite element model for mantle convection, Ph.D. thesis, Univ. of Calif., Los Angeles.

Baumgardner, J. R. (1985), Three dimensional treatment of convective flow in the Earth's mantle, *J. Stat. Phys.*, *39*, 501–511.

Baumgardner, J. R., and P. O. Frederickson (1985), Icosahedral discretization of the two-sphere, *SIAM J. Numer. Anal.*, *22*, 1107–1155.

Becker, T. W., J. B. Kellogg, and R. J. O'Connell (1999), Thermal constraints on the survival of primitive blobs in the lower mantle, *Earth Planet. Sci. Lett.*, *171*, 351–365.

Bina, C. R. (1998), Lower mantle mineralogy and the geophysical perspective, *Rev. Mineral.*, *37*, 205–239.

Brandon, A., R. Walker, J. Morgan, M. Norman, and H. Prichard (1998), Coupled ^{186}Os and ^{187}Os evidence for core-mantle interaction, *Science*, *280*, 1570–1573.

Bunge, H. P., and J. R. Baumgardner (1995), Mantle convection modelling on parallel virtual machines, *Comput. Phys.*, *9*(2), 207–215.

Bunge, H. P., M. A. Richards, and J. R. Baumgardner (1997), A sensitivity study of three-dimensional spherical mantle convection at 10^8 Rayleigh number: Effects of depth-dependent viscosity, heating mode, and an endothermic phase boundary, *J. Geophys. Res.*, *102*(B6), 11,991–12,007.

Cardin, P., and H. C. Nataf (1991), Nonlinear dynamic coupling observed near the threshold of convection in a 2-layer system, *Europhys. Lett.*, *14*, 655–660.

Cardin, P., H.-C. Nataf, and P. Dewost (1991), Thermal coupling in layered convection—Evidence for an interface viscosity control from mechanical experiments and marginal stability analysis, *J. Phys II*, *1*, 599–622.

Castle, J. C., and R. D. van der Hilst (2003a), Searching for seismic scattering off mantle interfaces between 800 km and 2000 km depth, *J. Geophys. Res.*, *108*(B2), 2095, doi:10.1029/2001JB000286.

Castle, J. C., and R. D. van der Hilst (2003b), Using ScP precursors to search for mantle structures beneath 1800 km depth, *Geophys. Res. Lett.*, *30*(8), 1422, doi:10.1029/2002GL016023.

Christensen, U. R., and A. Hofmann (1994), Segregation of subducted oceanic crust in the convecting mantle, *J. Geophys. Res.*, *99*, 19,867–19,884.

Christensen, U. R., and D. A. Yuen (1984), The interaction of a subducting lithospheric slab with a chemical or phase boundary, *J. Geophys. Res.*, *89*(B6), 4389–4402.

Courtillot, V., A. Davaille, J. Besse, and J. Stock (2003), Three distinct types of hotspots in the Earth's mantle, *Earth Planet. Sci. Lett.*, *205*, 295–308.

Cserepes, L., and M. Rabinowicz (1985), Gravity and convection in a 2-layer mantle, *Earth Planet. Sci. Lett.*, *76*, 193–207.

Davaille, A. (1999a), Simultaneous generation of hotspots and superswells by convection in a heterogeneous planetary mantle, *Nature*, *402*, 756–760.

Davaille, A. (1999b), Two layer thermal convection in miscible viscous fluids, *J. Fluid Mech.*, *379*, 223–253.

Davaille, A., F. Girard, and M. Le Bars (2002), How to anchor hotspots in a convecting mantle?, *Earth Planet. Sci. Lett.*, *203*, 621–634.

Davies, G. F. (1984), Geophysical and isotopic constraints on mantle convection: An interim synthesis, *J. Geophys. Res.*, *89*, 6017–6040.

Davies, G. F. (1988), Ocean bathymetry and mantle convection: 1. Large flow and hotspots, *J. Geophys Res.*, *93*, 10,467–10,480.

Davies, G. F. (1999), *Dynamic Earth: Plates, Plumes and Mantle Convections*, pp. 192–193, Cambridge Univ. Press, New York.

Davies, G. F., and M. Gurnis (1986), Interaction of mantle dregs with convection: Lateral heterogeneity at the core-mantle boundary, *Geophys. Res. Lett.*, *13*, 1517–1520.

DePaolo, D. J., and G. J. Wasserburg (1976), Inferences about mantle sources and mantle structure from variations of ^{147}Nd/^{144}Nd, *Geophys. Res. Lett.*, *3*, 743–746.

Deuss, A., and J. H. Woodhouse (2002), A systematic search for mantle discontinuities using SS-precursors, *Geophys. Res. Lett.*, *29*(8), 1249, doi:10.1029/2002GL014768.

Dziewonski, A., and D. L. Anderson (1981), Preliminary Reference Earth Model, *Phys. Earth Planet. Inter.*, *25*, 297–356.

Ellsworth, K., and G. Schubert (1988), Numerical models of thermally and mechanically coupled 2-layer convection of highly viscous fluids, *Geophys. J. Int.*, *93*, 347–363.

Forte, A. M., and J. X. Mitrovica (2001), Deep-mantle high-viscosity flow and thermochemical structure inferred from seismic and geodynamic data, *Nature*, *410*, 1049–1056.

Forte, A. M., J. X. Mitrovica, and A. Espesset (2002), Geodynamic and seismic constraints on the thermochemical structure and dynamics of convection in the deep mantle, *Philos. Trans. R. Soc. London, Ser. A*, *360*, 2521–2543.

Glatzmaier, G. A., and G. Schubert (1993), Three-dimensional spherical-models of layered and whole mantle convection, *J. Geophys. Res.*, *98*, 21,969–21,976.

Gonnermann, H. M., M. Manga, and A. M. Jellinek (2002), Dynamics and longevity of an initially stratified mantle, *Geophys. Res. Lett.*, *29*(10), 1399, doi:10.1029/2002GL014851.

Grand, S. P., R. D. van der Hilst, and S. Widiyantoro (1997), Global Seismic Tomography: A snapshot of convection in the Earth, *GSA Today*, *7*, 1–7.

Hager, B. H., R. W. Clayton, M. A. Richards, R. P. Comer, and A. M. Dziewonski (1985), Lower mantle heterogeneity, dynamic topography and the geoid, *Nature*, *313*, 541–545.

Helffrich, G. R., and B. J. Wood (2001), The Earth's mantle, *Nature*, *412*, 501–507.

Hoffman, A. W. (1997), Mantle geochemistry: The message from oceanic volcanism, *Nature*, *285*, 219–229.

Hofmann, A. W., and W. M. White (1982), Mantle plumes from ancient oceanic crust, *Earth Planet. Sci. Lett.*, *57*, 421–436.

Holmes, A. (1928), Continental drift: A review, *Nature*, *122*, 431–433.

Ishii, M., and J. Tromp (1999), Normal-mode and free-air gravity constraints on lateral variations in velocity and density of Earth's mantle, *Science*, *285*, 1231–1236.

Ishii, M., and J. Tromp (2001), Even-degree lateral variations in the Earth's mantle constrained by free oscillations and the free-air gravity anomaly, *Geophys. J. Int.*, *145*, 77–96.

Janney, P. E., J. D. Macdougall, J. H. Natland, and M. A. Lynch (2000), Geochemical evidence from the Pukapuka volcanic ridge system for a shallow enriched mantle domain beneath the south Pacific superswell, *Earth Planet. Sci Lett.*, *181*, 47–60.

Jellinek, A. M., and M. Manga (2002), The influence of a chemical boundary layer on the fixity, spacing and lifetime of mantle plumes, *Nature*, *418*, 760–763.

Jellinek, A. M., A. Lenardic, and M. Manga (2002), The influence of interior mantle temperature on the structure of plumes: Heads for Venus, Tails for the Earth, *Geophys. Res. Lett.*, *29*(11), 1532, doi:10.1029/2001GL014624.

Kawakatsu, H., and F. L. Niu (1994), Seismic evidence for a 920-km discontinuity in the mantle, *Nature*, *371*, 301–305.

Kellogg, L. H., B. H. Hager, and R. D. van der Hilst (1999), Compositional stratification of the lower mantle, *Science*, *283*, 1881–1884.

Kuo, C., and B. Romanowicz (2002), On the resolution of density anomalies in the Earth's mantle using spectral fitting of normal-mode data, *Geophys. J. Int.*, *150*, 162–179.

Lay, T., Q. Williams, and E. J. Garnero (1998), The core-mantle boundary layer and deep Earth dynamics, *Nature*, *392*, 461–468.

Le Bars, M., and A. Davaille (2002), Stability of thermal convection in two superimposed miscible viscous fluids, *J. Fluid Mech.*, *471*, 339–363.

Lenardic, A., and W. M. Kaula (1993), A numerical treatment of geodynamic viscous flow problems involving the advection of material interfaces, *J. Geophys. Res.*, *98*, 8243–8260.

Machetel, P., and P. Weber (1991), Intermittent layered convection in a model mantle with an endothermic phase-change at 670 km, *Nature*, *350*, 55–57.

Matyska, C., J. Moser, and D. A. Yuen (1994), The potential influence of radiative heat transfer on the formation of megaplumes in the lower mantle, *Earth Planet. Sci. Lett.*, *125*, 255–266.

McKenzie, D. P. (1969), Speculations on the consequences and causes of plate motions, *Geophys. J. R. Astron. Soc.*, *18*, 1–32.

Montagner, J. P. (1994), Can seismology tell us anything about convection in the mantle?, *Rev. Geophys.*, *32*, 115–137.

Montagner, J.-P., and B. L. N. Kennett (1996), How to reconcile body-wave and normal-mode reference earth modes, *Geophys. J. Int.*, *125*, 229–248.

Montague, N. L., and L. H. Kellogg (2000), Numerical models of a dense layer at the base of the mantle and implications for the geodynamics of D″, *J. Geophys. Res.*, *105*, 1101–1114.

Namiki, A., and K. Kurita (2003), Heat transfer and interfacial temperature of two-layered convection: Implications for the D″-mantle coupling, *Geophys. Res. Lett.*, *30*(1), 1023, doi:10.1029/2002GL015809.

Oldham, D. N. (2004), On the possibility of layered mantle convection—Numerical simulations in a spherical geometry, Ph.D. thesis, Cardiff Univ., Cardiff.

O'Nions, R. K., and E. R. Oxburgh (1983), Heat and helium in the Earth, *Nature*, *306*, 429–431.

O'Nions, R. K., N. M. Evensen, and P. J. Hamilton (1979), Geochemical modeling of mantle differentiation and crustal growth, *J. Geophys. Res.*, *84*, 6091–6101.

Resovsky, J. S., and M. H. Ritzwoller (1999), Regularization uncertainty in density models estimated from normal mode data, *Geophys. Res. Lett.*, *26*, 2319–2322.

Resovsky, J. S., and J. Trampert (2002), Reliable mantle density error bars: An application of the neighbourhood algorithm to normal-mode and surface wave data, *Geophys. J. Int.*, *150*(3), 665–672.

Richards, M. A., and B. H. Hager (1984), Geoid anomalies in a dynamic earth, *J. Geophys. Res.*, *89*, 5987–6002.

Richter, F. M., and D. P. McKenzie (1981), On some consequences and possible causes of layered mantle convection, *J. Geophys. Res.*, *86*, 6133–6142.

Schmalzl, J., and A. Loddoch (2003), Using subdivision surfaces and adaptive surface simplification algorithms for modeling chemical heterogeneities in geophysical flows, *Geochem. Geophys. Geosyst.*, *4*(9), 8303, doi:10.1029/2003GC000578.

Stegman, D. R., M. A. Richards, and J. R. Baumgardner (2002a), Effects of depth-dependent viscosity and plate motions on maintaining a relatively uniform mid-ocean ridge basalt reservoir in whole mantle flow, *J. Geophys. Res.*, *107*(B6), 2116, doi:10.1029/2001JB000192.

Stegman, D. R., A. M. Jellinek, S. A. Zatman, J. R. Baumgardner, and M. A. Richards (2002b), An early lunar core dynamo driven by thermochemical mantle convection, *Nature*, *421*, 143–146.

Tackley, P. J. (2000), Mantle convection and plate tectonics: Towards an integrated physical and chemical theory, *Science*, *288*, 2002–2007.

Tackley, P. J. (2002), Strong heterogeneity caused by deep mantle layering, *Geochem. Geophys. Geosyst.*, *3*(4), 1024, doi:10.1029/2001GC000167.

Tackley, P. J., and S. Xie (2002), The thermo-chemical structure and evolution of Earth's mantle: Constraints and numerical models, *Philos. Trans. R. Soc. London, Ser. A*, *360*, 2593–2609.

Tackley, P. J., D. J. Stevenson, G. A. Glatzmaier, and G. Schubert (1993), Effects of an endothermic phase-transition at 670 km depth in a spherical model of convection in the Earth's mantle, *Nature*, *361*, 699–704.

van der Hilst, R. D., and H. Karason (1999), Compositional heterogeneity in the bottom 1000 kilometers of Earth's mantle: Toward a hybrid convection model, *Science*, *283*, 1885–1888.

van der Hilst, R. D., S. Widiyantoro, and E. R. Engdahl (1997), Evidence for deep mantle circulation from global tomography, *Nature*, *386*, 578–584.

Van Keken, P. E., H. Schmeling, U. R. Christensen, D. Neumeister, and M. Doin (1997), A comparison of methods for the modeling of thermochemical convection, *J. Geophys. Res.*, *102*, 2477–2496.

Van Keken, P. E., E. H. Hauri, and C. J. Ballentine (2002), Mantle mixing: The generation, preservation and destruction of chemical heterogeneity, *Annu. Rev. Earth. Planet. Sci.*, *30*, 493–525.

Vidale, J. E., G. Schubert, and P. S. Earle (2001), Unsuccessful initial search for a midmantle chemical boundary with seismic arrays, *Geophys. Res. Lett.*, *28*, 859–862.

Vinnik, L., M. Kato, and H. Kawakatsu (2001), Search for seismic discontinuities in the lower mantle, *Geophys. J. Int.*, *147*, 41–56.

Wei-Jia, S., and A. M. Dziewonski (1991), Predominance of long-wavelength heterogeneity in the mantle, *Nature*, *352*, 121–126.

Wen, L. X., and D. L. Anderson (1995), The fate of slabs inferred from seismic tomography and 130 millions years of subduction, *Earth Planet. Sci. Lett.*, *133*, 185–198.

Wen, L. X., and D. L. Anderson (1997), Layered mantle convection: A model for geoid and topography, *Earth Planet. Sci. Lett.*, *146*, 367–377.

Yang, W. S. (1997), Variable viscosity thermal convection at infinite Prandtl number in a thick spherical shell, Ph.D. thesis, Univ. of Ill. at Urbana-Champaign.

Zindler, A., and S. Hart (1986), Chemical geodynamics, *Annu. Rev. Earth Planet. Sci.*, *14*, 493–570.